Low-Reynolds-number aerofoil boundary layer transition in large-scale free stream turbulence

Connor Toppings ond Serhiy Yarusevych o

¹Department of Mechanical and Mechatronics Engineering, University of Waterloo, Waterloo, ON N2L 3G1, Canada

Corresponding author: Serhiy Yarusevych, syarus@uwaterloo.ca

(Received 27 May 2025; revised 20 August 2025; accepted 23 September 2025)

The effects of high-intensity, large-scale free stream turbulence on the aerodynamic loading and boundary layer flow field development on a NACA 0018 aerofoil model were studied experimentally using direct force measurements and particle image velocimetry at a chord Reynolds number of 7×10^4 . An active turbulence grid was used to generate free stream turbulence intensities of up to 16 % at integral length scales of the order of the aerofoil chord length. Relative to the clean flow condition with a free stream turbulence intensity of 0.1 %, elevated levels of free stream turbulence intensity decrease the lift slope at low angles of attack, and increase the stall angle and maximum lift coefficient. At moderate angles of attack, high-intensity free stream turbulence causes large variations in the location of transition, with laminar flow occasionally persisting over 90 % of the chord length. At pre-stall angles of attack, high-intensity free stream turbulence causes intermittent massive separation. Variations in the extent of turbulence in the suction surface boundary layer are linked to fluctuations in effective angle of attack, suggesting that the observed variability in transition location is related to large-scale incoming flow disturbances impinging on the aerofoil model. A comparative analysis of the present results and those in previous studies for predominantly smaller integral length scales shows the importance of both the intensity and length scale of free stream turbulence on the flow development over the aerofoil.

Key words: aerodynamics, boundary layers, transition to turbulence

1. Introduction

Boundary layer transition in low-disturbance environments involves the exponential amplification of wave-like disturbances of the velocity field (Saric, Reed & Kerschen 2002).

© The Author(s), 2025. Published by Cambridge University Press. This is an Open Access article, distributed under the terms of the Creative Commons Attribution licence (https://creativecommons.org/licenses/by/4.0/), which permits unrestricted re-use, distribution and reproduction, provided the original article is properly cited.

The primary disturbance amplification mechanism in attached boundary layers is the Tollmien–Schlichting instability, which becomes active at a certain critical Reynolds number (Reed, Saric & Arnal 1996). In regions of adverse pressure gradient, the streamwise velocity profile develops an inflection point (Schlichting & Gersten 2017), which is sufficient to activate the Kelvin–Helmholtz instability mechanism regardless of Reynolds number (Reed *et al.* 1996). In boundary layers that separate due to an adverse pressure gradient, the spectrum of amplified disturbances is continuous from the attached boundary layer through to the separated shear layer (Michelis, Yarusevych & Kotsonis 2018).

Laminar boundary layer separation is common on lifting surfaces that operate at aerodynamically low chord Reynolds numbers $(Re_c = cu_\infty/\nu \le 5 \times 10^5)$, where c is the aerofoil chord length, u_{∞} is the free stream velocity and ν is the kinematic viscosity) (Carmichael 1981). When the disturbances in the separated laminar shear layer reach sufficiently high amplitudes, the shear layer rolls up and periodic vortex shedding ensues (Watmuff 1999). The frequency and wavenumber of the roll-up vortices correspond to those most amplified by the upstream flow (Boutilier & Yarusevych 2012c). At low levels of free stream turbulence intensity (FSTI), the roll-up vortices are spanwise coherent at formation (Hosseinverdi & Fasel 2019). Secondary instabilities eventually lead to threedimensional vortex deformations and transition to turbulence (e.g. Marxen, Lang & Rist 2013). If the increase in wall-normal momentum transfer due to transition is sufficient to overcome the adverse pressure gradient, the turbulent shear layer will reattach to the lifting surface, enclosing a region of recirculating flow known as a laminar separation bubble (LSB) (Tani 1964). Reattachment provides a substantial increase in lift-to-drag ratio relative to the case of separation without reattachment (Carmichael 1981). This scenario is typical for $Tu \lesssim 2\%$ (where $Tu = \sigma_u/u_\infty$ is the turbulence intensity and σ_u is the standard deviation of the streamwise velocity) (Istvan & Yarusevych 2018). In addition to the turbulence intensity, another parameter characterising free stream turbulence is the streamwise integral length scale (Λ_{ux}) (e.g. Cao, Ting & Carriveau 2011; Ravi et al. 2012). In large-scale free stream turbulence ($\Lambda_{ux} \gtrsim c$), intermittent LSB formation and massive separation may occur due to fluctuations in effective angle of attack (Ravi et al. 2012; Herbst et al. 2018, 2020; Kay, Richards & Sharma 2020; Wang & Xiao 2021).

At higher levels of FSTI, transition may occur prior to saturation of the primary instability through a process called bypass transition (Reshotko 2001). Bypass transition usually involves the formation of low-frequency streamwise-elongated disturbances called streaks within the pre-transitional boundary layer (Matsubara & Alfredsson 2001). There is a consensus that the streak-formation process depends on the receptivity of the leading-edge region (e.g. Nagarajan, Lele & Ferziger 2007; Ovchinnikov, Choudhari & Piomelli 2008; Zhao & Sandberg 2020). The leading-edge receptivity acts as a low-pass filter, enabling low-frequency disturbances to penetrate into the boundary layer while attenuating high-frequency content from the outer flow (Matsubara & Alfredsson 2001; Hernon, Walsh & Mceligot 2007).

Streaks are produced by the stretching and tiling of vortices into the streamwise direction by the presence of the leading edge (Nagarajan *et al.* 2007). The streamwise vortices cause convection of lower momentum fluid away from the wall and higher momentum fluid towards the wall, forming low- and high-speed streaks, respectively (Zhao & Sandberg 2020). Consequently, high-speed streaks occur nearer to the wall than low-speed streaks (Mandal, Venkatakrishnan & Dey 2010). Transverse velocity fluctuations at the leading edge can also cause the formation of streaks (Ovchinnikov *et al.* 2008). The shape of the leading edge influences the location of bypass transition, with earlier transition occurring for larger leading edge radii (Nagarajan *et al.* 2007).

As the streaks convect downstream within the boundary layer, their streamwise length and velocity fluctuation amplitude increase (Matsubara & Alfredsson 2001; Mandal *et al.* 2010). The variance of the streamwise velocity fluctuations in the boundary layer caused by the streaks grows linearly with respect to the streamwise distance from the leading edge (Kendall 1985), reaching $\sim 0.1 u_{\infty}^2$ prior to transition (Matsubara & Alfredsson 2001). As the streaks develop, the magnitude of the peak negative velocity fluctuations become greater than the peak positive velocity fluctuations (Hernon *et al.* 2007).

Secondary instability of the shearing regions between high- and low-speed streaks eventually causes streak breakdown and the formation of turbulent spots (Mandal et al. 2010). Regardless of formation mechanism, hairpin and streamwise vortices are a common feature of turbulent spots (Ovchinnikov et al. 2008; Nolan & Walsh 2012). The subsequent growth and merging of turbulent spots leads to a fully turbulent boundary layer (Matsubara & Alfredsson 2001). For a given level of turbulence intensity, there is a specific ratio of the streamwise integral length scale (Λ_{ux}) to the boundary layer thickness (δ) at the location of transition that optimally promotes transition (Fransson & Shahinfar 2020). Mamidala, Weingärtner & Fransson (2022) reported that this ratio is between 10 and 15. At very high turbulence intensities (\sim 20 %) and large length scales ($\Lambda_{ux} > 1000\nu/u_{\infty}$), turbulent spots may form without streaks as precursors (Ovchinnikov et al. 2008; Zhao & Sandberg 2020).

Elevated FSTI increases the initial amplitudes of disturbances in the boundary layer (Istvan & Yarusevych 2018) and broadens their energy content across a wider frequency range (Jaroslawski *et al.* 2023). For LSBs on aerofoils at low Reynolds numbers, this causes earlier transition and reattachment, leading to a reduction in LSB length and thickness (Jaroslawski *et al.* 2023). As a consequence of the reduction in wall-normal extent of the LSB, disturbance growth rates in the separated shear layer are reduced (Istvan & Yarusevych 2018). The frequency band of unstable disturbances in the pretransitional shear layer shifts to higher frequencies with increasing FSTI due to the decrease in boundary layer thickness and increase in edge velocity (Jaroslawski *et al.* 2023). At moderate levels of FSTI, low- and high-speed streaks cause deformations of the shear layer roll-up vortices, reducing their spanwise coherence (Istvan, Kurelek & Yarusevych 2018; Yu *et al.* 2024; Canepa *et al.* 2025). At higher levels of FSTI (Tu > 4%), streak amplitudes may be sufficient to prevent separation entirely (Jaroslawski *et al.* 2023) and bypass transition dominates over the Kelvin–Helmholtz instability mechanism (Hosseinverdi & Fasel 2019).

At very low Reynolds numbers ($Re_c < 5 \times 10^4$) and moderate angles of attack ($2^\circ < \alpha < 7^\circ$) where the separated laminar shear layer does not transition before reaching the trailing edge, elevated FSTI can lead to LSB formation and an increase in lift coefficient (Hrynuk *et al.* 2024). At higher Reynolds numbers where LSBs naturally form at relatively low FSTI, an increase in FSTI typically leads to a reduction in LSB length due to expedited transition and reattachement (e.g. Simoni *et al.* 2017; Jaroslawski *et al.* 2023). The reduction in LSB size caused by elevated FSTI has a substantial effect on aerofoil performance. Accelerated transition under conditions of increased FSTI causes more gradual stall (Damiola *et al.* 2023) and an increase in stall angle and maximum lift coefficient (Istvan *et al.* 2018). At pre-stall angles of attack, increased FSTI causes a reduction in lift because the low-pressure plateau associated with the LSB decreases in length (Istvan & Yarusevych 2018).

Most previous studies considering the effect of elevated FSTI on flows around aerofoils and finite wings primarily focused on the effect of turbulence intensity (e.g. Hoffmann 1991; Laitone 1997; Sytsma & Ukeiley 2013; Wang *et al.* 2014; Maldonado *et al.* 2015; Istvan *et al.* 2018; Li & Hearst 2021; Damiola *et al.* 2023; Hrynuk *et al.* 2024), whereas the

effect of the streamwise integral length scale (Λ_{ux}) is less well understood (Jaroslawski et al. 2023). The effect of the integral length scale is more subtle than the turbulence intensity (Hosseinverdi & Fasel 2019) and is stronger at lower free stream turbulence intensities (Cao et al. 2011). The integral length scale has a negligible affect on the range of unstable frequencies in the boundary layer (Jaroslawski et al. 2023). However, when the ratio of the integral length scale to the boundary layer thickness is closest to that most optimal for bypass transition, higher initial amplitudes of boundary layer disturbances lead to earlier transition, reducing LSB length (Wang & Xiao 2021; Jaroslawski et al. 2023). For lifting surfaces at aerodynamically relevant Reynolds numbers, this occurs when $A_{\mu\nu} \ll c$. Increasing Λ_{ux}/δ above the optimal ratio leads to an increase in lift slope and maximum lift coefficient, and a decrease in stall angle (Delnero et al. 2005; Cao et al. 2011; Ravi et al. 2012). The largest amplitude variations in suction surface pressure coefficients occur when $\Lambda_{ux} \approx c$ (Vita et al. 2020). If the integral length scale of the free stream turbulence is near the characteristic length scale of natural vortex shedding from a stalled aerofoil, a substantial increase in load fluctuations may occur relative to smaller or larger integral length scales (Thompson *et al.* 2023).

The majority of previous studies on boundary layer transition in aerodynamically low-Reynolds-number flows have been limited to free stream turbulence intensities below 10 % and integral length scales less than the aerofoil chord (e.g. Yaras 2002; Cao et al. 2011; Coull & Hodson 2011; Mahallati et al. 2012; Wang et al. 2014; Simoni et al. 2017; Istvan et al. 2018; Hosseinverdi & Fasel 2019; Li & Hearst 2021; Jaroslawski et al. 2023). A limited number of studies have considered turbulence intensities of 10 % or greater and integral length scales longer than the aerofoil chord. Among those studies, Watkins, Ravi & Loxton (2010), Ravi et al. (2012), Kay et al. (2020) and Devinant, Laverne & Hureau (2002) focused on characterisation of the pressure distribution and loading on wings and aerofoils, whereas Herbst, Kähler & Hain (2018) and Herbst, Hain & Kähler (2020) also reported on the time- and conditionally averaged boundary layer development on the suction surface. For Tu = 7% and 12%, Ravi et al. (2012) found that increasing the integral length scale at constant Tu from c to approximately 2c increased the maximum lift coefficient of a flat plate aerofoil. Although Herbst et al. (2020) observed an increase in maximum lift coefficient when increasing A_{ux} from 0.5c to c at Tu = 10 % for an SD7003 wing, a further increase in A_{ux} to 2c did not cause a significant change in maximum lift coefficient. The difference between the results of Ravi et al. (2012) and Herbst et al. (2020) suggests that the lifting surface geometry may influence the effect of the integral length scale on aerodynamic loading. The effect of aerofoil geometry on the lift coefficient in high-intensity, large-scale free stream turbulence was investigated by Kay et al. (2020) for a symmetrical and cambered aerofoil for $1.3 \% \le Tu \le 15 \%$ at $5 \times 10^4 \le Re_c \le 2 \times 10^5$ with streamwise integral length scales of the order of the aerofoil chord. They inferred from surface pressure measurements that fluctuations in effective angle of attack beyond the static stall angle lead to intermittent dynamic stall events associated with the shedding of leading edge vorticity. These events corresponded to transient increases in lift coefficient which were stronger for the symmetric aerofoil than for the cambered aerofoil (Kay et al. 2020). Devinant et al. (2002) studied the loading on a wind turbine aerofoil at FSTIs of up to 16%, and reported a decrease in the lift slope and a more gradual stall behaviour with increasing FSTI. The flow field around a fully stalled aerofoil with $4\% \le Tu \le 16\%$ and $\Lambda_{ux} \sim c$ was investigated by Sicot et al. (2006), who found that the variations in the suction surface boundary layer separation location and wake vortex shedding Strouhal number were insensitive to FSTI. Although the effect of free stream turbulence on aerodynamic loading has been studied by several authors, the dynamics of the boundary layer transition process that cause the observed

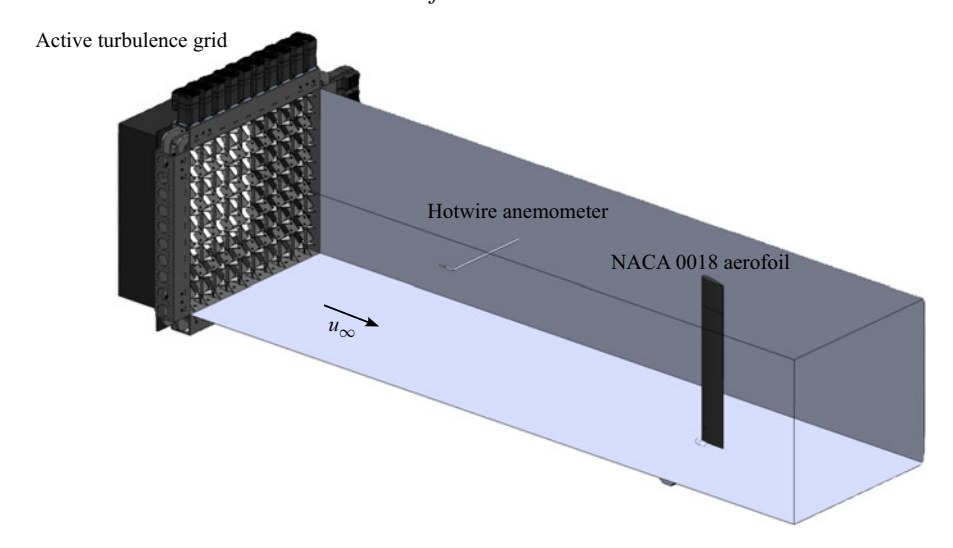


Figure 1. Experimental setup.

changes in lifting surface performance in large-scale high-intensity free stream turbulence remains relatively unexplored. One consistent observation in experiments involving large-scale high-intensity turbulence has been intermittent separation and LSB formation (Ravi et al. 2012; Herbst et al. 2018, 2020; Kay et al. 2020). This is in contrast to flows at relatively moderate turbulence intensities and length scales, in which the LSB is typically suppressed intransiently due to bypass transition (Istvan et al. 2018; Hosseinverdi & Fasel 2019).

Better understanding of the transition mechanisms in large-scale high-intensity free stream turbulence is necessary to improve the performance and control of small unmanned aerial vehicles (Mueller & DeLaurier 2003) and small wind turbines (Wood 2011) that operate in atmospheric flows with turbulence intensities of 10 % or greater (Watkins et al. 2010) and a wide range of energy-containing length scales (Wyngaard 1992). The most detrimental length scales of free stream turbulence for the safe and controlled operation of aircraft are expected to be those of the order of the aerofoil chord length (Watkins et al. 2006). Therefore, the objective of the present work is to quantify the effects of high-intensity, large-scale free stream turbulence on aerofoil performance at low Reynolds numbers and to correlate changes in the boundary layer transition dynamics to fluctuations in the oncoming flow. To achieve this objective, wind tunnel experiments were performed using a NACA 0018 aerofoil model with an active turbulence grid placed upstream of the test section to generate controlled free stream turbulence intensities and integral length scales. Direct aerodynamic force measurements and suction surface boundary layer velocity field measurements were employed to quantify aerofoil performance and boundary layer transition dynamics, respectively.

2. Experimental methods

2.1. *Model and facility*

Experiments were conducted in the recirculating wind tunnel at the University of Waterloo. The experimental set-up is illustrated in figure 1. The test section is square, with a width and height of 0.61 m and a length of 2.44 m. The free stream velocity was set based on a calibration of the pressure drop across the 9:1 contraction located upstream of the test

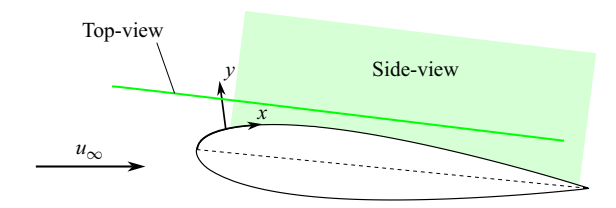


Figure 2. PIV measurement plane configurations and coordinate system definitions. The z axis is in the out-of-plane direction in the sense of a right-handed coordinate system.

section measured using a Setra model 239 pressure transducer. The relative uncertainty in the mean free stream velocity is estimated to be 3 % (95 % confidence). The NACA 0018 aerofoil used in this study had a chord length of c = 0.1 m and spanned the height of the test section. To facilitate direct force measurements, the aerofoil model was structurally isolated from the test section walls with gaps of approximately 4 mm at each end. The regions of three-dimensional flow caused by the presence of the tip gaps are expected to be limited to within one chord length of the ends of the model (Marchman 1987; Toppings & Yarusevych 2022). With the aspect ratio 5 model used in this study, the gaps at the tips of the model are expected to have negligible influence on the spanwise uniformity of the flow at the midspan of the model where the particle image velocimetry (PIV) measurements were performed. The aerofoil was machined from aluminium, polished with 1000 grit sandpaper and anodised black to minimise light reflections. A stepper motor controlled rotary table with a resolution of 0.05° was used to set the angle of attack of the aerofoil. The aerofoil was connected to the rotary table through a 6-axis load cell. The absolute accuracy in force measurements from the load cell was 0.1 N. All experiments were performed at a chord Reynolds number of $Re_c = 7.0 \times 10^4$, corresponding to a mean free stream velocity of $\overline{u_{\infty}} = 10.7 \,\mathrm{m \, s^{-1}}$.

2.2. Flow measurements

Two-component PIV measurements were performed over the suction surface of the aerofoil in two measurement planes shown in figure 2. The side-view measurement plane was normal to the span of the aerofoil and located at the midspan of the model, and the top-view measurement plane was tangent to, but offset from, the suction surface of the aerofoil. The minimum distance between the top-view measurement plane and the aerofoil was 2 mm. The PIV data are presented in a surface attached coordinate system whose origin is at the midspan leading edge, with the streamwise (x) axis tangent to the suction surface, the wall-normal (y) axis normal to the aerofoil surface and the spanwise (z) axis parallel to the span in the sense of a right-handed coordinate system. Particle images were obtained using a Photron Fastcam Nova R3-4K camera with a 105 mm focal length macro lens at an aperture of f/2.8. The flow was seeded with water–glycol fog particles of diameter O(1 μm). The particles were illuminated by a Photonics Industries DM20-527 Nd:YLF pulsed laser operating in frame straddling mode, with a pulse separation of 15 µs. Image acquisition and processing were performed using the LaVision DaVis 10 software. Particle images were pre-processed using temporal minimum subtraction with a window length of 8 images. Local intensity normalisation with window sizes of 4×4 pixels and 32×32 pixels was used for the side-view and top-view images, respectively. Vector calculation was performed using an iterative cross-correlation algorithm with window deformation (Scarano & Riethmuller 2000). The vector fields for both measurement planes were post-processed using universal outlier detection (Westerweel & Scarano 2005). For the side-view configuration, vectors were deleted if the correlation coefficient was less

than 0.5. For the top-view configuration, vectors were deleted if the correlation peak ratio was less than 1.6. For both measurement planes, the maximum particle displacement was approximately 15 px, and the initial and final correlation window sizes were 24 px \times 24 px and 16 px \times 16 px, with 75 % window overlap for the final iteration. The vector pitch of the final velocity fields was 0.0009c and 0.0007c for the side- and top-view PIV configurations, respectively. A summary of the parameters for each PIV configuration is provided in table 1.

In addition to the instantaneous velocity vector fields computed from image pairs, time-mean velocity fields were also calculated using the average correlation method (Meinhart, Wereley & Santiago 2000) for improved spatial resolution in the boundary layer for the side-view configuration. The average correlation method involves averaging the correlation maps from all image pairs before determining the mean particle displacement from the correlation peak. For the average correlation method, the mean velocity field obtained from the standard PIV method was used to estimate the initial displacements and the final correlation window size was $4 \text{ px} \times 4 \text{ px}$ with 75 % window overlap. The vector pitch of the mean velocity fields from the average correlation method was 0.0002c.

For the side-view configuration, PIV measurements were taken at sampling frequencies of 3.9 kHz and 0.1 kHz to obtain time-resolved and statistical data, respectively. The size of the field of view and the sampling period were varied for different flow conditions and sampling frequencies, and are tabulated in the Appendix. To correct for relative motion between the aerofoil and the camera due to model vibrations at elevated FSTI, each side-view PIV image was aligned with the first image in the sequence based on the cross-correlation of the illuminated aerofoil surface between images. For the top-view configuration, only non-time-resolved PIV measurements were acquired at 0.1 kHz. The size of the top-view field of view was $0.76c \times 0.42c$, and the sampling period was 11.99 s.

The uncertainty in the instantaneous PIV measurements was estimated using the correlation statistics method (Wieneke 2015). The root-mean-square (r.m.s.) uncertainty (95 % confidence) in the instantaneous streamwise (u) and wall-normal (v) velocity components was estimated to be less than $0.06\overline{u_{\infty}}$ outside of the aerofoil boundary layer. Adjacent to the aerofoil surface, stronger velocity gradients and light reflections increased the r.m.s. uncertainty to no more than $0.3\overline{u_{\infty}}$. For the top-view configuration, the uncertainty in the instantaneous streamwise velocity component was less than $0.04\overline{u_{\infty}}$ over the majority of the field of view, increasing to no more than $0.18\overline{u_{\infty}}$ where the top-view measurement plane intersected the separated shear layer due to strong velocity gradients. The uncertainty in the instantaneous spanwise velocity measurements from the top-view configuration is also estimated to be less than $0.04\overline{u_{\infty}}$, increasing to no more than $0.12\overline{u_{\infty}}$ in the separated shear layer. The uncertainty of quantities derived from the PIV measurements was estimated using the methods described by Moffat (1988) and Sciacchitano & Wieneke (2016).

2.3. Free stream turbulence generation

Free stream turbulence was generated using an active turbulence grid consisting of 10 horizontal and 10 vertical steel shafts of diameter 7.94 mm upon which were fixed square aluminium wings with a diagonal of 56.96 mm (figure 1). The wings adjacent to the test section walls were triangular. The rotation of each shaft was controlled by a dedicated stepper motor. The free stream turbulence intensity and streamwise integral length scale were estimated at the location of the aerofoil leading edge in the empty test section based on measurements with a single normal hotwire anemometer probe. During tests with the aerofoil mounted in the test section, free stream velocity fluctuations were measured

Parameter	Value			
Camera Lens focal length Laser pulse separation Aperture Light source Particles Maximum particle image displacement Initial correlation window	Photron fastcam nova R3-4K 105 mm $15 \mu \text{s}$ $f/2.8$ Photonics DM20-527 Nd:YLF pulsed laser Water–glycol fog $15 px$ $24 px \times 24 px$			
	Side-view Top-view			
Magnification factor	0.29		0.35	
	Instantaneous	Average correlation		
Final correlation window Vector pitch Final correlation window overlap	16 px × 16 px 0.0009c 75 %	4 px × 4 px 0.0002 <i>c</i> 75 %	$16 \mathrm{px} \times 16 \mathrm{px} \\ 0.0007 c \\ 75 \%$	
	Non-time-resolved T		Time-resolved	
Sampling frequency	0.1 kHz		3.9 kHz	

Tu [%] Λ_{ux}/c	Flapping mode		Rotation mode	
111 [70]	I_{ux}/c				
		Amplitude [deg.]	Mean frequency [Hz]	Mean speed [revs ⁻¹]	Mean time interval [s]
0.1	0.1				
4	1	19	5.6		
4	2	19	2.6		
7	1	37	6.7		
7	2	35	3.1		
13	1			8.38	0.93
16	2			2.45	0.93

Table 1. PIV measurement parameters.

Table 2. Free stream turbulence conditions and active grid motion parameters.

with a single normal hotwire anemometer probe positioned at the centre of the test section 10c upstream of the aerofoil. A summary of the turbulence intensity and integral length scales investigated is provided in table 2, and figure 3 presents the power spectral density (PSD) of free stream velocity fluctuations ($\mathcal{P}_f(u_\infty')$) for each case. The spectra were obtained using Welch's method (Welch 1967) with a Hamming window of length 2^{16} samples and 50 % window overlap from 300 s of data sampled at 20 kHz. Turbulence intensities and integral length scales were computed after bandpass filtering the hotwire signal. The low-frequency cutoff of the filter was $0.005u_\infty/c$ and the high-frequency cutoff was the frequency at which the PSD fell below the measurement noise floor of $\mathcal{P}_f(u_\infty') = 10^{-8}$. The relative uncertainty in Tu was estimated to be less than 10 % (i.e. the uncertainty for Tu = 13 % is $< \pm 1.3$ %), following the approach outlined by Yavuzkurt (1984). The streamwise integral length scale was estimated from the streamwise integral

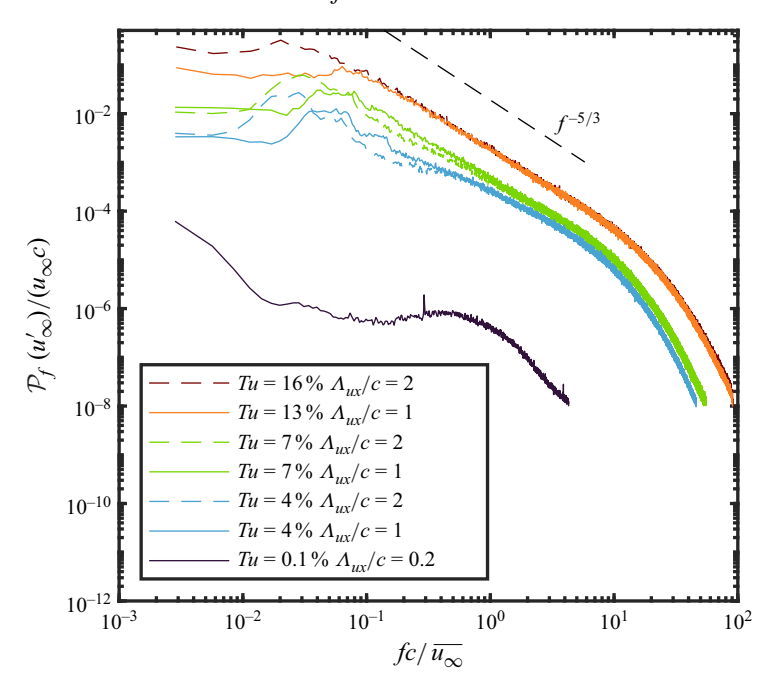


Figure 3. Free stream turbulence spectra.

time scale using the frozen turbulence hypothesis (Taylor 1938):

$$\Lambda_{ux} = \overline{u_{\infty}} \int_{0}^{\infty} \rho_{u_{\infty}' u_{\infty}'}(t) \, \mathrm{d}t, \tag{2.1}$$

where $\rho_{u_{\infty}'u_{\infty}'}(t)$ is the temporal autocorrelation coefficient of the free stream velocity fluctuations. Because estimates of $\rho_{u_{\infty}'u_{\infty}'}(t)$ obtained from finite length experimental data may not converge to 0 for large t, the streamwise integral time scale was computed by integrating an exponential fit to $\rho_{u'_{\infty}u'_{\infty}}(t)$ (Schrader 1993; Gomes-Fernandes, Ganapathisubramani & Vassilicos 2012). The relative uncertainty in the streamwise integral length scale estimated from the variance of the streamwise integral length scale computed over shorter (60 s) segments of the hotwire recordings was less than 10 %. The spanwise integral length scale (Λ_{wz}) was estimated from an exponential fit to the spatial autocorrelation coefficient (e.g. Gomes-Fernandes et al. 2012; Kurelek, Lambert & Yarusevych 2016) of the spanwise velocity fluctuations of the top-view PIV measurements outside of the boundary layer near the leading edge of the aerofoil. The spanwise velocity fluctuations were used for this estimate because they are expected to be less affected by the blocking effect of the aerofoil (Hunt 1973) than the streamwise velocity fluctuations. The estimated values of Λ_{wz} were of the order of 0.1c. In other investigations of active (Hearst & Lavoie 2015) and passive (Valente & Vassilicos 2011) grid-generated turbulence, integral length scales in the spanwise direction and those for spanwise velocity components in the streamwise direction have also been reported to be substantially smaller than the streamwise integral length scale.

Two different shaft motion protocols were used to generate different turbulence intensities. The grid motion parameters for these two protocols are summarised in table 2. For Tu = 4% and 7%, the grid was operated in flapping mode such that the shafts oscillated about a mean angle of attack of zero. The amplitude and frequency of the shafts'

oscillation were varied depending on the desired turbulence intensity and integral length scale, respectively. The frequency of oscillation of each shaft was varied according to a top-hat probability distribution to avoid exciting a single frequency of velocity fluctuations. The bounds of the top-hat distribution were $\pm 1/2$ of the mean frequency. To minimise the influence of oscillation frequency on the energy spectrum of the free stream turbulence, the oscillation frequency of each shaft was continually re-sampled from the uniform distribution. To generate higher FSTI (Tu = 13% and Tu = 16%), the grid was operated in rotation mode, where the shafts performed complete rotations at random rotational velocities for random intervals of time. The rotation speeds and time intervals were varied using top-hat probability distributions with bounds set at $\pm 1/2$ of the mean rotation speed and time interval, respectively. Measurements were also taken with the active turbulence grid removed from the test section. This condition is termed the clean flow and the FSTI for the clean flow was Tu = 0.1%.

2.4. Data processing techniques

2.4.1. Proper orthogonal decomposition

The snapshot method of proper orthogonal decomposition (POD) is employed in the present work to identify coherent structures from PIV data (Sirovich 1987). POD decomposes the velocity data u(x, t) into a set of $k \in \{1, ..., N\}$ spatial modes $\phi_k(x)$, modal energies λ_k^2 and temporal coefficients $a_k(t)$:

$$\boldsymbol{u}(\boldsymbol{x},t) = \sum_{k=1}^{N} \boldsymbol{\phi}_{k}(\boldsymbol{x}) \lambda_{k} a_{k}(t). \tag{2.2}$$

Although the mean velocity field is often subtracted from the velocity data before performing the POD, in this work, the mean is not subtracted because we require the POD modes to contain information about the mean flow (e.g. Chen, Reuss & Sick 2012) for the entropy-based transition detection method detailed in § 2.4.2. The POD can be obtained from the singular value decomposition of the snapshot matrix whose rows represent the spatial locations of velocity measurements and whose columns represent the individual snapshots (e.g. Chatterjee 2000). The uncertainty of the computed modal energies was estimated using the method described by Epps & Krivitzky (2019). Two different PODs were performed on the PIV data using different formulations of the snapshot matrix.

The first POD, termed the velocity profile POD (P-POD), was performed independently on the data obtained at each x-grid location in the side-view PIV field of view (i.e. x = y in (2.2), thus the data snapshots were the u and v velocity profiles at each streamwise location). This POD produced a set of spatial modes, modal energies and temporal coefficients for each x location that describe the shape and time evolution of the velocity profile at that location.

The second POD, termed the velocity field POD (F-POD), was performed on the data from the entire side-view PIV field of view (i.e. $x = [x, y]^T$ in (2.2), thus the data snapshots were the two-dimensional u and v velocity fields). This POD produced a single set of spatial modes and temporal coefficients for each PIV measurement run that describe the two-dimensional flow-field development.

2.4.2. Transition detection

The transition from laminar to turbulent states involves an increase in the disorder of a flow (Lesieur 2008). The degree of disorder can be quantified by applying the concept of

entropy from information theory (Shannon 1949) to the POD (Aubry, Guyonnet & Lima 1991; Abdelsamie, Janiga & Thévenin 2017; Uruba 2019). An ordered, laminar flow can be described by a relatively small number of POD modes, whereas a turbulent flow typically requires a relatively greater number of POD modes to account for the same fraction of the total kinetic energy (e.g. Taira *et al.* 2017). Thus, more information is required to describe a turbulent flow than a laminar flow. The quantity of information contained in the POD modes that describe a flow can be expressed in terms of entropy (Aubry *et al.* 1991). The entropy of the POD is zero when the velocity field can be exactly represented by a single POD mode. The entropy is maximum if the kinetic energy of the flow is evenly distributed among all POD modes. Thus, the entropy of the flow is related to the relative energy distribution of the POD modes. Aubry *et al.* (1991) defined a global entropy S_g that is a constant for a given snapshot matrix and spatial entropy $S_g(t)$ that is a function of time. The global entropy, S_g , is given by (Aubry *et al.* 1991)

$$S_g = -\sum_{k=1}^{N} p_{g,k} \ln(p_{g,k}), \tag{2.3}$$

where $p_{g,k}$ are the relative modal energies, computed as

$$p_{g,k} = \frac{\lambda_k^2}{\sum_{k=1}^{N} \lambda_k^2}.$$
 (2.4)

The global entropy is zero if the flow is steady and the global entropy is maximised if all data snapshots are uncorrelated. The spatial entropy of the flow at a given instant in time is given by (Aubry *et al.* 1991)

$$S_s(t) = -\sum_{k=1}^{N} p_{s,k}(t) \ln(p_{s,k}(t)), \qquad (2.5)$$

where $p_{s,k}(t)$ are computed as

$$p_{s,k}(t) = \frac{a_k^2(t)\lambda_k^2}{\sum_{k=1}^N a_k^2(t)\lambda_k^2}.$$
 (2.6)

Note that, unlike Aubry *et al.* (1991), the relative energies $p_{s,k}(t)$ in the definition of the spatial entropy have been computed using $a_k^2(t)\lambda_k^2$ instead of $a_k(t)\lambda_k$ to maintain symmetry with the definition of global entropy (e.g. Li, Yano & Lin 2019). The spatial entropy is zero if only one $a_k(t)$ is non-zero, that is, if the velocity field at time t can be exactly represented by a single POD mode. The spatial entropy is maximum if $a_k^2(t)\lambda_k^2$ is constant for all k, that is, if the kinetic energy of the flow is evenly distributed among all modes at time t. Since turbulent flows are characterised by a redistribution of energy from larger to smaller spatio-temporal scales, the global and spatial entropies increase as the flow becomes more turbulent.

The global entropy computed from the P-POD quantifies the degree of disorder in both the wall-normal direction and time at each x location. The spatial entropy of the P-POD at each x location quantifies the degree of spatial disorder of the velocity profile as a function of time. Since the spatial entropy can be computed separately on the P-POD for each x location, the spatial disorder of the velocity profile can be plotted in the x-t plane. The global entropy of the F-POD quantifies the degree of disorder of the two-dimensional

flow field within the entire field of view in space and time. The spatial entropy of the F-POD quantifies the degree of spatial disorder of the PIV flow-field as a function of time.

The main advantage of using entropy to measure the degree of turbulence in the flow compared with traditional methods of calculating the intermittency factor (e.g. Hedley & Keffer 1974) is that the computation of entropy from the POD is an entirely data-driven procedure that does not require the computation of temporal derivatives from time-resolved data. However, to distinguish laminar from turbulent flow, selection of a threshold that separates these two flow regimes is unavoidable. Although Abdelsamie *et al.* (2017) demonstrated that transition occurs at similar values of global entropy for numerical simulations of widely varying flow configurations, in the present study, the entropy threshold separating laminar and turbulent flow regimes was determined empirically from the PIV data. The selection of the transition threshold is detailed in § 3.3.1.

Unlike methods that define the instantaneous transition location using integral boundary layer quantities (e.g. Dellacasagrande *et al.* 2020) or Reynolds stresses computed over a sliding temporal window (e.g. Toppings & Yarusevych 2023), defining the instantaneous transition location using the spatial entropy from the P-POD (2.5) does not require temporal windowing. Consequently, the spatial entropy from the P-POD has the potential to more precisely differentiate between unsteady laminar and turbulent flows.

3. Results

3.1. Aerodynamic forces

Lift and drag coefficient polars for the aerofoil under all tested conditions of free stream turbulence are presented in figure 4. The lift coefficient from thin aerofoil theory is also plotted for comparison. The maximum solid blockage was less than 7%, for which the errors in lift coefficients due to blockage are expected to be less than 10% (Boutilier & Yarusevych 2012a). The reduction in lift coefficient relative to a true two-dimensional aerofoil, due to the presence of the gaps between the tips of the model and the test section walls, is estimated to be of the order of 0.1 based on the results of Marchman (1987). In the clean flow (Tu = 0.1%), the pre-stall lift is highly nonlinear with respect to the angle of attack and exceeds that predicted by thin aerofoil theory for $\alpha \le 6^\circ$. Nonlinear lift at moderate angles of attack is typical of aerofoils operating at aerodynamically low Reynolds numbers (e.g. Ohtake, Nakae & Motohashi 2007; Winslow *et al.* 2018) and is attributed to the increased local suction that occurs due to the presence of a short LSB (Tani 1964). Bursting of the LSB for $\alpha > 8^\circ$ leads to an abrupt stall, decreasing lift and increasing drag.

When the FSTI is increased to 4 %, the stall angle increases substantially and the lift at low angles of attack is relatively more linear, in agreement with the effects of moderate FSTI observed in previous studies (Kay et al. 2020; Hrynuk et al. 2024). These changes are attributed to the free stream turbulence causing expedited transition, which reduces the size of the LSB and its associated pressure plateau (e.g. Istvan et al. 2018). There are no significant differences in pre-stall lift as the FSTI increases from Tu = 4% to 7 %, but the post-stall decrease in lift becomes less abrupt. At Tu = 13 %, there is a substantial reduction in lift at pre-stall angles of attack, and the post-stall decrease in lift and increase in drag become notably more gradual. These changes are attributed to a continued reduction in the extent of separated flow at very high free stream turbulence intensities, which will be explored in § 3.3. The observed decrease in lift slope and more gradual stall with increasing FSTI are in agreement with the measurements of Devinant et al. (2002). There is no significant change in aerofoil performance between integral

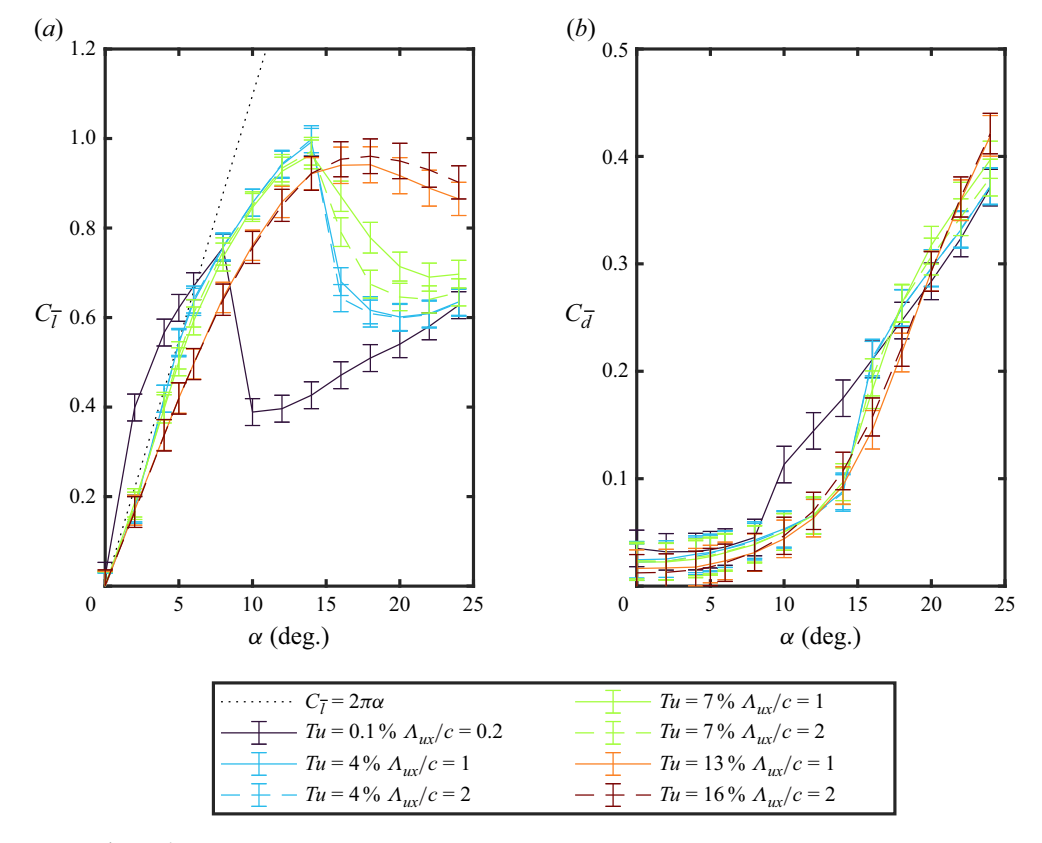


Figure 4. (a) Lift and (b) drag coefficients. Error bars denote uncertainty (95 % confidence).

length scales of $\Lambda_{ux}/c = 1$ and 2 at pre-stall angles of attack (compare solid and dashed lines). For Tu = 7%, there is a decrease in post-stall lift at the larger length scale. It is speculated that this decrease may be caused by a delay in transition due to a reduction in the amplitudes of velocity fluctuations in the free stream at the length scales to which the boundary layer is most receptive.

3.2. Overview of boundary layer transition

To investigate the mechanisms responsible for the changes in aerofoil performance at high FSTI with large integral length scales, side-view PIV measurements of the suction surface boundary layer were obtained at $\alpha = 5^{\circ}$, which is within 2° of the angle of maximum lift to drag ratio for all tested cases, and at $\alpha = 12^{\circ}$, which represents an angle at which performance is severely degraded at low FSTI.

The boundary layer transition process on the suction surface of the aerofoil at $\alpha = 5^{\circ}$ is illustrated using instantaneous snapshots of spanwise vorticity ($\omega = \partial v/\partial x - \partial u/\partial y$) in figure 5 for Tu = 0.1%, 7% and 13%. The snapshots are separated by $0.06c/\overline{u_{\infty}}$ and are ordered with increasing time from top to bottom. The spanwise vorticity was computed from the circulation on the contour of the eight neighbouring velocity vectors around each PIV grid point (Reuss *et al.* 1989) and smoothed using a 3×3 spatial average. Instantaneous streamwise velocity and spanwise vorticity fields from time-resolved PIV measurements for Tu = 0.1, 4%, 7% and 13% at $\Lambda_{ux}/c = 1$ are available in supplementary movie 1 available at https://doi.org/10.1017/jfm.2025.747.

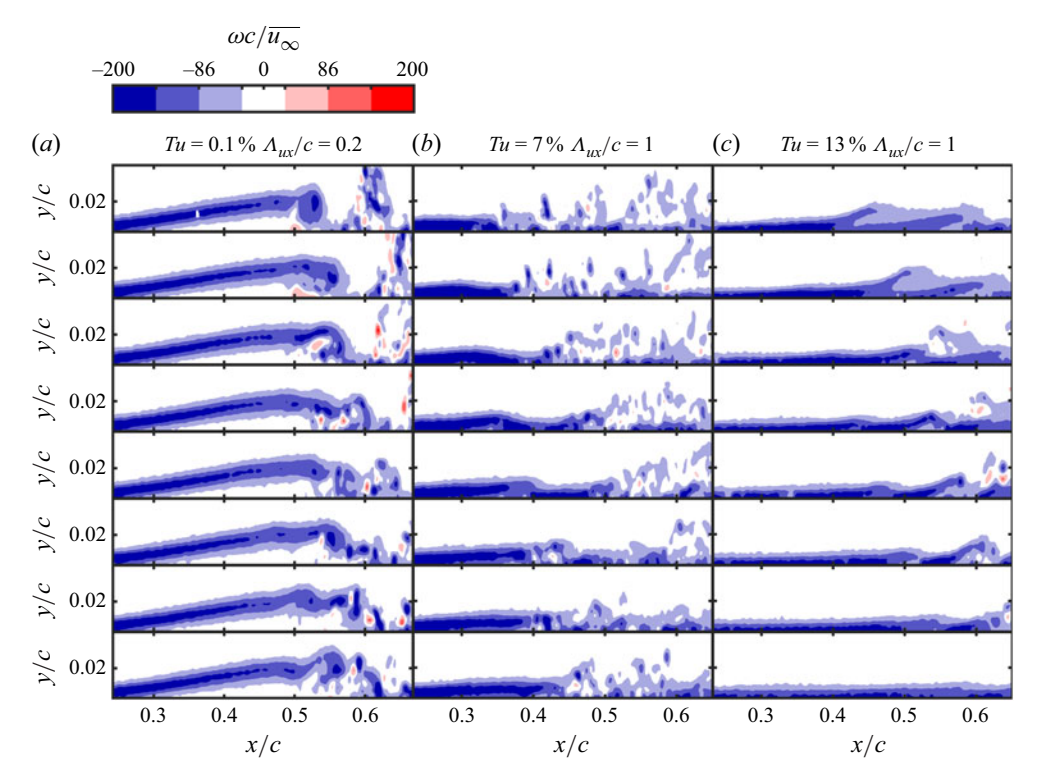


Figure 5. Instantaneous snapshots of spanwise vorticity. Time increases from top to bottom and the snapshot separation is $0.06c/u_{\infty}$.

In the clean flow (figure 5a), due to the relatively low amplitudes of incoming disturbances, the boundary layer remains laminar over a substantial distance, leading to laminar boundary layer separation in the region of adverse pressure gradient. The separated laminar shear layer rolls up into relatively large-scale coherent vortices near x/c = 0.55 as a consequence of the Kelvin-Helmholtz instability mechanism (e.g. Ho & Huerre 1984; Dovgal, Kozlov & Michalke 1994). The increase in wall-normal momentum transport produced by the vortices leads to reattachment and a turbulent boundary layer develops as the spanwise vortices break down into small-scale turbulence for x/c > 0.6. This transition scenario is consistent with the features typical of short LSBs (Marxen & Henningson 2011). The location of shear layer roll-up is observed to remain relatively consistent in time.

With increasing FSTI (figures 5b and 5c), higher amplitudes of boundary layer disturbances are generally expected to lead to earlier transition in a time-averaged sense (e.g. Simoni *et al.* 2017; Jaroslawski *et al.* 2023). The location of transition in the vorticity field snapshots can be inferred from the onset of relatively small-scale spatial variations in spanwise vorticity. Interestingly, the snapshots in figure 5 show that substantially greater variations in the location of transition occur with increasing FSTI. For Tu = 13%, the variations in transition location are large enough to cause the boundary layer to occasionally remain laminar across the entire PIV field of view (figure 5c, bottom panel). It is likely that these variations are a consequence of the relatively large integral length scale of the free stream turbulence, which leads to temporal variations in effective angle of attack and incoming flow velocity. The relationship between the variations in transition

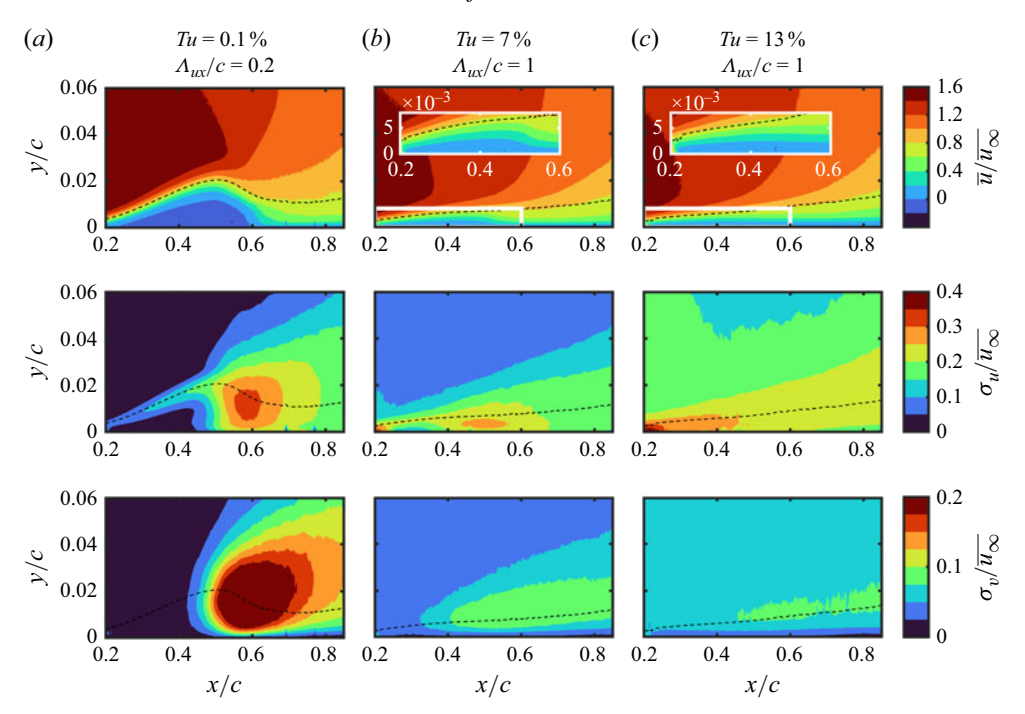


Figure 6. Mean streamwise velocity fields (top row), and standard deviation of streamwise (middle row) and wall-normal (bottom row) velocity fields for $\alpha = 5^{\circ}$. Dashed lines, $\overline{\delta^*}$.

location and large-scale free stream velocity fluctuations will be investigated in detail in § 3.5.

In addition to the location of transition, the FSTI also affects the development of vortical structures formed in the transition process (e.g. Hosseinverdi & Fasel 2019). Whereas the roll-up vortices formed in the clean flow are relatively large and coherent, the breakdown of the laminar shear layer at Tu = 7% involves less organised, finer-scale structures (figure 5b). At Tu = 13%, the inclined regions of increased vorticity within the boundary layer are consistent with the lift-up of low-speed streaks that eventually decay into turbulent spots (Nolan & Walsh 2012). The presence of streaks is evidence that bypass transition occurs at Tu = 13%. The snapshots presented in figure 5 illustrate that large-scale free stream turbulence can cause substantial changes in the mean flow development and the transition dynamics relative to the clean flow.

3.3. Mean flow development

Mean streamwise velocity (\overline{u}) , standard deviation of streamwise velocity (σ_u) and standard deviation of wall-normal velocity (σ_v) fields for $Tu=0.1\,\%$, $7\,\%$ and $13\,\%$ at an integral length scale of $\Lambda_{ux}/c=1$ are presented in figures 6 and 7 for $\alpha=5^\circ$ and 12° , respectively. The mean streamwise velocity fields were obtained from the average correlation method, whereas the other fields were computed as the average of the instantaneous PIV vector fields. Also plotted is the mean displacement thickness, defined as $\overline{\delta^*} = \int_0^{\overline{\delta}} (1 - \overline{u}/\overline{u_e}) \, \mathrm{d}y$, where δ is taken as the wall-normal distance to the location of the maximum streamwise velocity (u_e) at a given x location. The inset plots in figures $\delta(b)$, $\delta(c)$, $\delta(c)$, $\delta(c)$, and $\delta(c)$ show the near-wall structure of the mean flow with an enlarged $\delta(c)$ scale. The results for $\delta(c)$ are similar to those for $\delta(c)$ and are not shown for brevity. Likewise, there

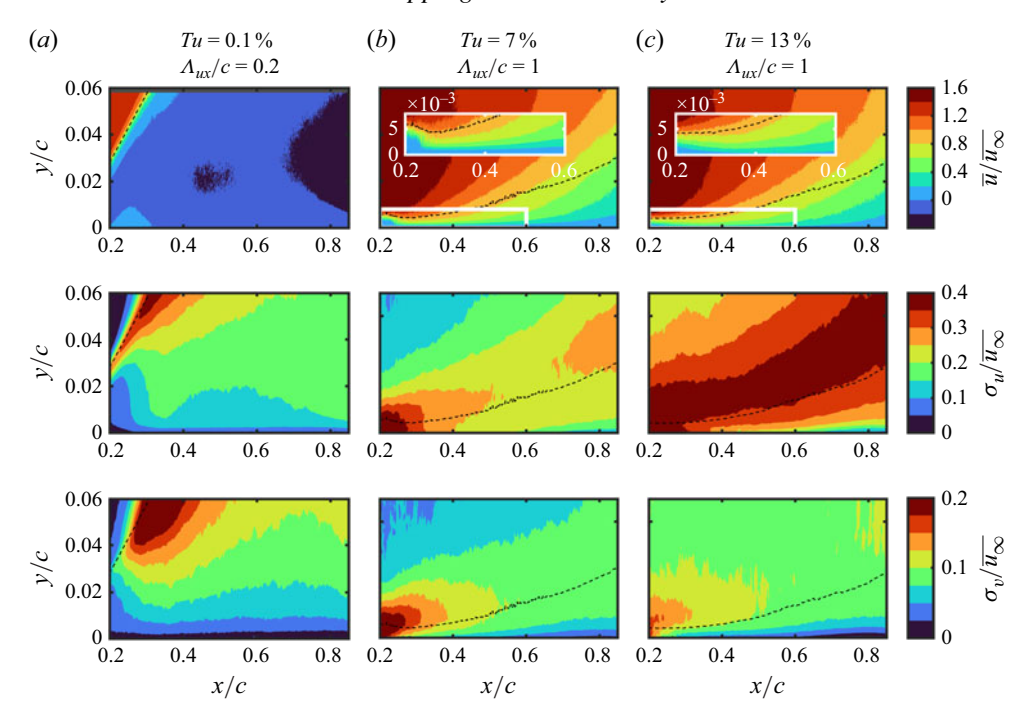


Figure 7. Mean streamwise velocity fields (top row), and standard deviation of streamwise (middle row) and wall-normal (bottom row) velocity fields for $\alpha = 12^{\circ}$. Dashed lines, $\overline{\delta^*}$.

are no notable differences between the mean and fluctuating flow fields for $\Lambda_{ux}/c = 2$ and those shown for $\Lambda_{ux}/c = 1$, consistent with the measured lift coefficients (figure 4).

The measurements in the clean flow for $\alpha = 5^{\circ}$ (figure 6a) show the development of a relatively thick LSB on the suction surface of the aerofoil. The two darkest blue contours in the mean streamwise velocity plot outline the extent of mean reverse flow in the LSB, with separation at x/c = 0.25 and reattachment at x/c = 0.58. Transition of the separated shear layer is evidenced by the rapid increase in velocity fluctuations that occurs near the location of maximum bubble thickness (x/c = 0.49). The ratio of the lengths of the laminar and turbulent portions of the LSB is 2.7, suggesting that this LSB should be classified as short (Marxen & Henningson 2011).

At $\alpha=5^\circ$ and Tu=7% (figure 6b), the reverse flow region is nearly eliminated. However, the increase in streamwise velocity at $y/c\approx 0.0025$ for 0.5 < x/c < 0.55 is similar to the flow structure seen near the reattachment location in the clean flow and suggests that a thin LSB may intermittently form at Tu=7%. Furthermore, the local maximum in streamwise velocity fluctuations and increase in wall-normal velocity fluctuations that occurs near x/c=0.5 are consistent with LSB formation, since vortex shedding from the separated shear layer is expected to cause an increase in streamwise and wall-normal velocity fluctuations near the reattachment location (Lengani *et al.* 2014; Dellacasagrande *et al.* 2020). Evidence of vortex shedding in the POD spatial modes for these conditions will be discussed in § 3.4.

At $\alpha=5^\circ$ and Tu=13% (figure 6c), the FSTI is sufficiently high that the presence of an LSB is not evident in the mean or fluctuating velocity fields. The region of increased streamwise velocity fluctuations near the wall for $x/c \le 0.5$ without a corresponding increase in wall-normal velocity fluctuations suggests that transition at this level of FSTI is dominated by streak formation and breakdown rather than separated shear layer roll-up.

The mean flow fields presented in figure 6 show that increasing the FSTI progressively decreases the extent of separated flow at $\alpha = 5^{\circ}$. Because the LSB produces a low-pressure plateau in the surface pressure distribution (Horton 1968), the decrease in lift coefficient with increasing FSTI is largely attributed to the reduction in streamwise extent of the LSB.

The reason for the substantial change in aerofoil performance at $\alpha = 12^{\circ}$ with varying FSTI (figure 4) is evident from the mean flow fields for this angle of attack presented in figure 7. For the clean flow (figure 7a), the reduced lift and increased drag are due to massive separation from the suction surface of the aerofoil. In this case, the amplitudes of free stream disturbances are too low for transition to occur rapidly enough to enable reattachment.

At Tu = 7%, the extent of separation is substantially reduced because of more rapid boundary layer transition (figure 7b). However, a thin region of mean reverse flow was detected at the upstream end of the field of view for Tu = 7% and the streamwise velocity contours in the inset are consistent with those expected near the reattachment location of an LSB. Thus, a thin laminar separation bubble persists on the aerofoil for Tu = 7%. The presence of the LSB is consistent with the region of stronger wall-normal velocity fluctuations near the aerofoil surface for x/c < 0.2. The persistence of mean laminar separation up to at least Tu = 7% is attributed to the relatively low Reynolds number and strong adverse pressure gradient for the aerofoil at $\alpha = 12^\circ$. At Tu = 13%, no reverse flow was detected in the PIV measurements (figure 7c). However, the increase in streamwise velocity near the wall and plateau in δ^* for x/c < 0.4 suggest that a thin LSB may form upstream of the field of view.

3.3.1. Mean transition

In this section, the relationship between transition and time-averaged suction surface boundary layer properties is explored. It serves to define a transition threshold for the entropy-based transition detection method that is consistent with other boundary layer transition indicators commonly applied in low-Reynolds-number flows over aerofoils. The entropy-based method is used because it is desired to characterise instantaneous variations in the transition location in § 3.4 without requiring temporal windowing for calculation of Reynolds shear stresses or integral boundary layer parameters. Figures 8(a) and 8(b) present the Reynolds shear stress $(-\overline{u'v'})$ measured at $y = \overline{\delta^*}$ for $\alpha = 5^\circ$ and 12°, respectively. The shape factors $(H = \overline{\delta^*}/\overline{\theta})$, where $\overline{\theta} = \int_0^{\overline{\delta}} \overline{u}/\overline{u_e}(1 - \overline{u}/\overline{u_e}) \, dy)$ for $\alpha = 5^\circ$ and 12° are plotted in figures 8(c) and 8(d), respectively.

Because a rapid increase in the magnitude of the Reynolds shear stress is indicative of transition, several transition criteria for low-Reynolds-number boundary layers have been formulated based on the Reynolds shear stress (e.g. Lang *et al.* 2004; Ol *et al.* 2005; Burgmann & Schröder 2008). Moreover, the streamwise location of maximum Reynolds shear stress has been shown to occur near the location of reattachment in LSBs (e.g. Lengani *et al.* 2017). The location where $-\overline{u'v'}$ first exceeds $0.001\overline{u_e^2}$ is indicated by the dashed lines in figures 8(*a*) and 8(*b*). This threshold for $-\overline{u'v'}$ is based on the transition threshold used by Ol *et al.* (2005) and Hain, Kähler & Radespiel (2009). Other researchers have used the location of maximum shape factor to define the mean location of transition in LSBs (e.g. Michelis, Yarusevych & Kotsonis 2017; Dellacasagrande *et al.* 2020). The locations of the most upstream local maximum of the shape factor are indicated by the dotted lines in figures 8(*c*) and 8(*d*).

At $\alpha = 5^{\circ}$, a rapid increase in -u'v' begins near x/c = 0.44 for the clean flow condition (figure 8a), which agrees well with the location of maximum shape factor for the clean flow (figure 8d). A similar correlation between the locations of most rapid Reynolds shear stress

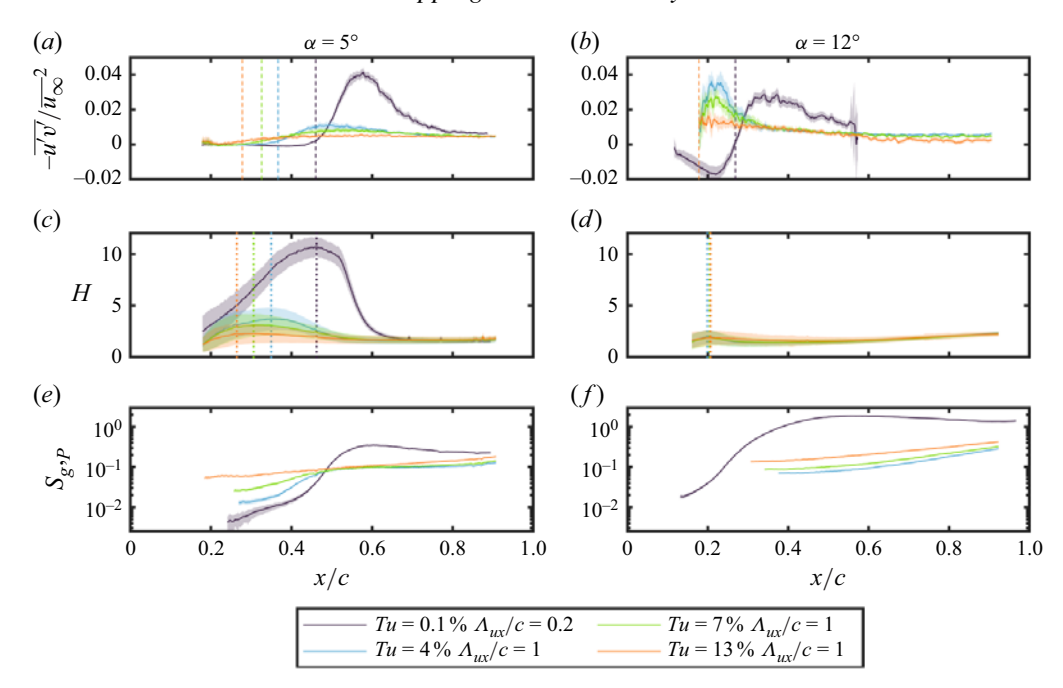


Figure 8. (a,b) Reynolds shear stress at $y = \overline{\delta^*}$, (c,d) shape factor and (e,f) global entropy from P-POD at (a,c,e) $\alpha = 5^\circ$ and (b,d,f) $\alpha = 12^\circ$. Dashed lines, $-\overline{u'v'} = 0.001\overline{u_e}^2$; dotted lines, maximum shape factor; shaded areas, uncertainty (95 % confidence).

growth and maximum shape factor is also apparent from the results at Tu = 4% and 7% for $\alpha = 5^{\circ}$. Relative to the clean flow, the locations of maximum Reynolds shear stress and shape factor for Tu = 4% and 7% are shifted upstream, indicating earlier transition. The continued presence of a maximum in the Reynolds shear stress distribution for Tu = 4% and 7% provide further evidence of the presence of a thin LSB for elevated FSTI at $\alpha = 5^{\circ}$. Notably, there is also reasonable agreement between the Reynolds shear stress transition location criterion and the location of maximum shape factor for Tu = 13%, despite the absence of measurable reverse flow for this condition (figure 6c).

At $\alpha=12^\circ$ and Tu=0.1%, the flow is massively separated and transition occurs near x/c=0.3, where there is a rapid increase in Reynolds shear stress (figure 8b). When the FSTI is increased to Tu=4% and Tu=7%, the maximum Reynolds shear stress occurs near the upstream end of the field of view. The location of the maximum in $-\overline{u'v'}$ for these conditions suggests that the boundary layer separates and transitions upstream of the field of view and reattaches near x/c=0.25, supporting the assertion made previously that the wall-normal velocity fluctuations in this region (figures 6b and 6c) are related to vortex shedding from an LSB. For $\alpha=12^\circ$, the shape factor for the clean flow is not plotted since it cannot be accurately estimated when the separated shear layer is outside of the PIV field of view. Although it is within the experimental uncertainty, for the cases of elevated FSTI at $\alpha=12^\circ$, there is a local maximum followed by a decrease in shape factor near x/c=0.25 that is consistent with boundary layer transition occurring near the upstream end of the PIV field of view in an LSB.

The mean transition locations determined from the Reynolds shear stress threshold and the location of the first local maximum of the shape factor are in reasonable agreement for all considered flow conditions, and indicate an upstream movement of the mean transition location with increasing FSTI and angle of attack. However, it is desired to characterise

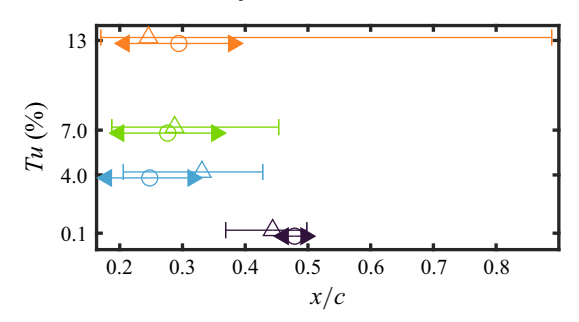


Figure 9. Locations of maximum shape factor (Δ) and mean transition location (\circ) for $\alpha = 5^{\circ}$, $\Lambda_{ux}/c = 1$. Arrows denote standard deviation, error bars denote uncertainty (95 % confidence).

instantaneous variations in the transition location without requiring temporal windowing or time-resolved data. For this purpose, an entropy-based transition criterion is used.

Streamwise distributions of global entropy computed from the P-POD $(S_{g,P})$ are plotted in figures 8(e) and 8(f) for the clean flow and elevated FSTI at $\alpha = 5^{\circ}$ and 12°, respectively. Because noise in the PIV measurements of the thin boundary layer at the upstream end of the field of view contributes to erroneously high values of entropy in that region, the global entropy is only plotted downstream of the location of minimum global entropy. For the clean flow at both $\alpha = 5^{\circ}$ and 12° , there is a relatively rapid increase in global entropy near the transition locations identified from the Reynolds shear stress threshold. There is also a more rapid increase in the global entropy near the locations of transition identified from the shape factor for Tu = 4% and Tu = 7% at $\alpha = 5^{\circ}$. This suggests that a transition threshold can be defined based on the global entropy. We choose to define the entropy threshold for transition $(S_{g,t})$ as the value of the global entropy at the location of maximum shape factor at $\alpha = 5^{\circ}$, since the location of maximum shape factor can be objectively measured for each level of FSTI. A specific threshold for each level of FSTI is used to mitigate the influence of the entropy of the free stream turbulence on boundary layer transition detection. The instantaneous transition criterion can be expressed as $S_{s,P} > S_{g,t}$. For Tu = 13 % at $\alpha = 5^{\circ}$, an obvious increase in the slope of the global entropy does not occur near the location of maximum shape factor. However, it will be shown that the intermittency factor distributions determined with the entropy threshold defined from the location of maximum shape factor at $\alpha = 5^{\circ}$ are in qualitative agreement with the observed transition dynamics for each flow condition investigated. To make estimation of the transition location (x_t) more robust to noise in the PIV measurements, we require that the instantaneous transition criterion be met over a total cumulative distance of at least 0.15c downstream of the location where the criterion was first met. Furthermore, x_t was smoothed with a moving median filter with window length $0.14c/\overline{u_{\infty}}$. By applying the transition threshold to the spatial entropy of the P-POD, turbulent flow can be identified as a function of time and streamwise location.

The mean transition locations determined from the instantaneous entropy-based transition criterion $S_{s,P} > S_{g,t}$ are compared with the location of maximum shape factor in figure 9 for $\alpha = 5^{\circ}$ and $A_{ux}/c = 1$, where the mean transition location falls within the field of view for all levels of FSTI investigated. The standard deviations of the transition locations (σ_{x_t}) are indicated by the arrows and the uncertainty in the locations of maximum shape factor are indicated by the error bars. The mean transition locations computed from the entropy-based criterion are all within the uncertainty intervals of the locations of maximum shape factor. When the FSTI is increased from Tu = 0.1% to 4%, there is a significant upstream movement in the transition location, expected to result from

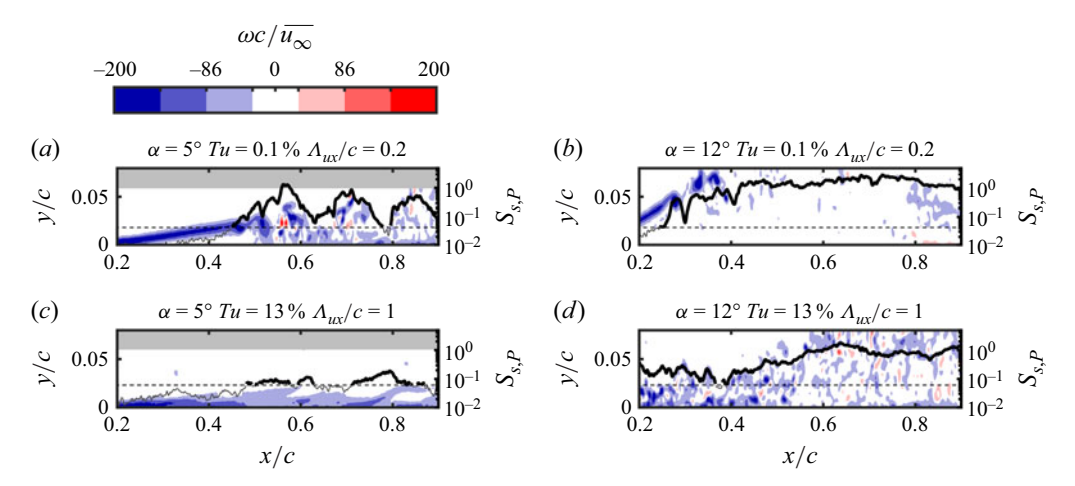


Figure 10. Instantaneous spanwise vorticity. Grey areas are outside the PIV field of view. Thick solid line, $S_{s,P}$ from P-POD in turbulent regions; thin solid line, $S_{s,P}$ from P-POD in laminar regions; dashed line, $S_{g,t}$.

bypass transition (e.g. Jaroslawski et al. 2023). However, the differences in mean transition locations among the cases of elevated FSTI determined using the entropy-based criterion are sensitive to the chosen transition thresholds, since the streamwise increase in entropy for these cases is more gradual (figure 8e). It should be noted that the limited streamwise extent of the field of view is a significant source of bias in the estimates of $\overline{x_t}$ and σ_{x_t} . Specifically, upstream excursions of x_t from the field of view at elevated FSTI bias the estimates of $\overline{x_t}$ downstream of their true locations and reduce the measured σ_{x_t} . Therefore, we refrain from drawing definitive conclusions about the change in mean transition locations between cases of elevated FSTI using the spatial entropy method. However, a more detailed exploration of the variations in the transition location in § 3.4 will show that the instantaneous transition location becomes more variable with increasing FSTI. At $\alpha = 12^{\circ}$, the mean transition location $(\overline{x_t})$ is upstream of the PIV field of view for all cases except the clean flow, for which it is located at $\overline{x_t}/c = 0.22$. Increasing the integral length scale to $\Lambda_{ux}/c=2$ produced no substantial changes in the locations of maximum shape factor or in $\overline{x_t}$ and its standard deviation. The following discussion explores the unsteady transition dynamics responsible for the variations in transition location.

3.4. Transition dynamics

The effect of the adverse pressure gradient, which is stronger at higher angles of attack, on the instantaneous transition dynamics at low and high FSTIs is visualised using the contours of instantaneous spanwise vorticity for Tu = 0.1% and 13% in figure 10. At both angles of attack for Tu = 0.1% (figures 10a and 10b), the separated laminar shear layer rolls up into relatively large-scale coherent vortices. At $\alpha = 5^{\circ}$ (figure 10a), an LSB forms, but at $\alpha = 12^{\circ}$ (figure 10b), the developing turbulent shear layer is unable to overcome the adverse pressure gradient and remains separated. At Tu = 13% (figures 10c and 10d), separation is suppressed due to bypass transition. The inclined structures at x/c = 0.5 and 0.8 in (figure 10c) are evidence of streak formation (Nolan & Walsh 2012) at the lower angle of attack. For Tu = 13% and $\alpha = 12^{\circ}$ (figure 10d), the stronger adverse pressure gradient causes earlier breakdown to small-scale turbulence within the boundary layer (e.g. Litvinenko et al. 2005) and no evidence of streaks is observed in this snapshot.

The relationship between vortical structures in the transitional boundary layer and the spatial entropy computed from the P-POD at each streamwise location is demonstrated in

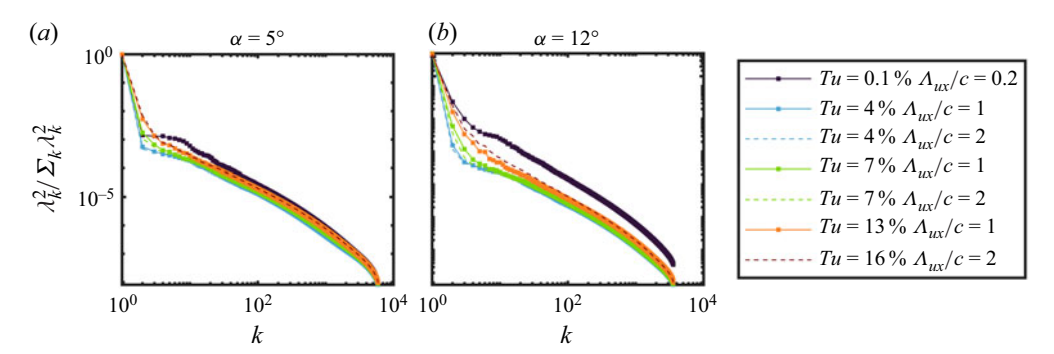


Figure 11. Relative energy of POD modes from F-POD.

figure 10. Relative to the laminar flow in the upstream portion of the LSB at $\alpha = 5^{\circ}$ and Tu = 0.1% (figure 10a), entropy is increased by the presence of small-scale turbulence (figure 10d), streaks (figure 10c) and breakdown of shear layer roll-up vortices (figure 10a). The relationship between these flow features and the computed spatial entropy confirms that the entropy tends to increase as the boundary layer transitions from laminar to turbulent states. Qualitatively, the transition thresholds (dashed lines in figure 5) demarcate reasonably well more laminar and more turbulent flow regions in various aerofoil operating conditions.

In § 3.3, the persistence of an LSB at elevated FSTI was inferred from the time-averaged flow-fields. Another indicator of the presence of an LSB is the periodic shedding of roll-up vortices from the separated shear layer near the location of mean reattachment. These coherent vortices can be characterised from their associated spatial F-POD modes (Legrand, Nogueira & Lecuona 2011; Lengani *et al.* 2014). Furthermore, the effect of FSTI on the most energetic coherent structures in the boundary layer can be elucidated from a comparison of the F-POD spatial modes corresponding to different flow conditions.

The relative modal energies for the F-POD $(\lambda_k^2/\sum_k \lambda_k^2)$, which describe the proportion of the flow's kinetic energy that is associated with each spatial mode, are presented in figure 11. The F-POD was performed on the non-time-resolved PIV measurements because these measurements cover a larger field of view. The streamwise component of the first ten spatial modes $(\phi_k(x))$ are presented in figures 12 and 13 for angles of attack of $\alpha = 5^\circ$ and 12°, respectively, for the clean flow and for elevated FSTI with $\Lambda_{ux}/c = 1$. The spatial modes for $\Lambda_{ux}/c = 2$ (not shown for brevity) are similar to those for $\Lambda_{ux}/c = 1$ and their relative energy content is also similar as shown in figure 11. Thus, a change in integral length scale from $\Lambda_{ux}/c = 1$ to 2 does not cause a substantial change in the spatial structure or relative energy content of coherent structures in the aerofoil boundary layer. Since the POD was performed without subtracting the mean flow field, the first F-POD mode, which contains over 85 % of the total energy in all cases, describes a flow field that is similar but not identical to the mean flow (e.g. Chen *et al.* 2012). The higher modes, which each contain less than 4 % of the total energy, describe spatially coherent velocity fluctuations whose spatial scale decreases with increasing mode index.

For the clean flow at $\alpha = 5^{\circ}$ (figure 12a), spatial modes 3–10 display spatially periodic velocity fluctuations beginning near the location of maximum LSB thickness, which are typical of vortex shedding from an LSB (e.g. Lengani *et al.* 2014; Lengani & Simoni 2015). At Tu = 4% (figure 12b), similar spatially periodic structures are present in the near-wall region of modes 4–10, providing further evidence of vortex shedding from a thin LSB under these operating conditions. Mode 2 for Tu = 4% describes a variation in

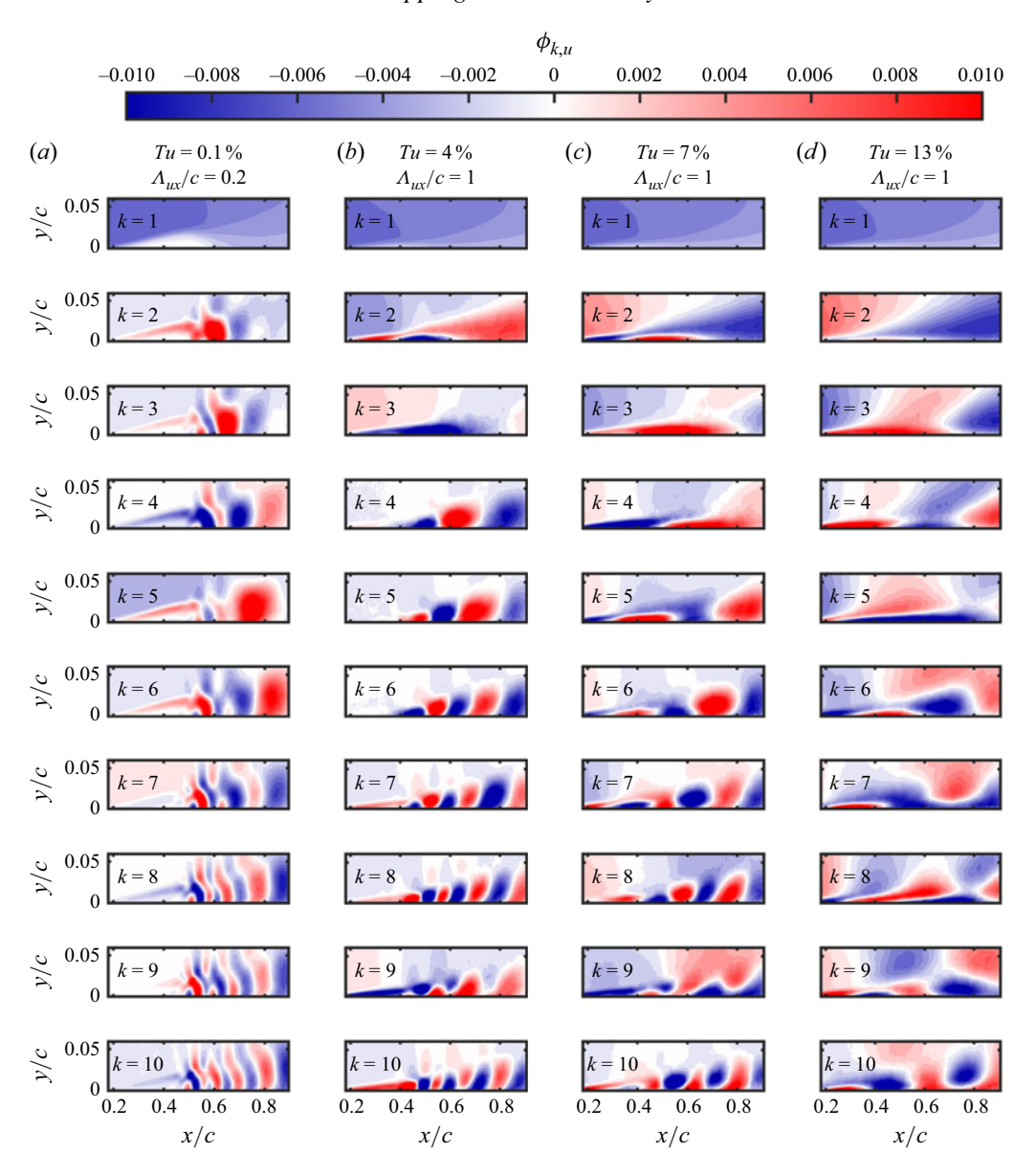


Figure 12. Streamwise component of POD spatial modes for $\alpha = 5^{\circ}$ and $\Lambda_{ux}/c = 1$.

the streamwise velocity gradient of the outer flow that is correlated to a modulation of the boundary layer. This mode is consistent with the expected response of an LSB to a change in pressure gradient. For example, if the time coefficient of this mode is positive, this mode describes a streamwise acceleration of the outer flow. The associated reduction in adverse pressure gradient would be expected to delay separation, transition and reattachment, leading to a downstream movement of the LSB, and this is consistent with the increase in streamwise velocity near the wall for x/c < 0.4 and reduction in streamwise velocity near the wall for 0.4 < x/c < 0.65 present in this spatial mode. Accounting for the reversal of sign, the similarity of the second spatial modes for the cases of Tu = 4%, 7% and 13% suggests that a thin LSB may intermittently form in all of these cases. Indeed, mode 10 for

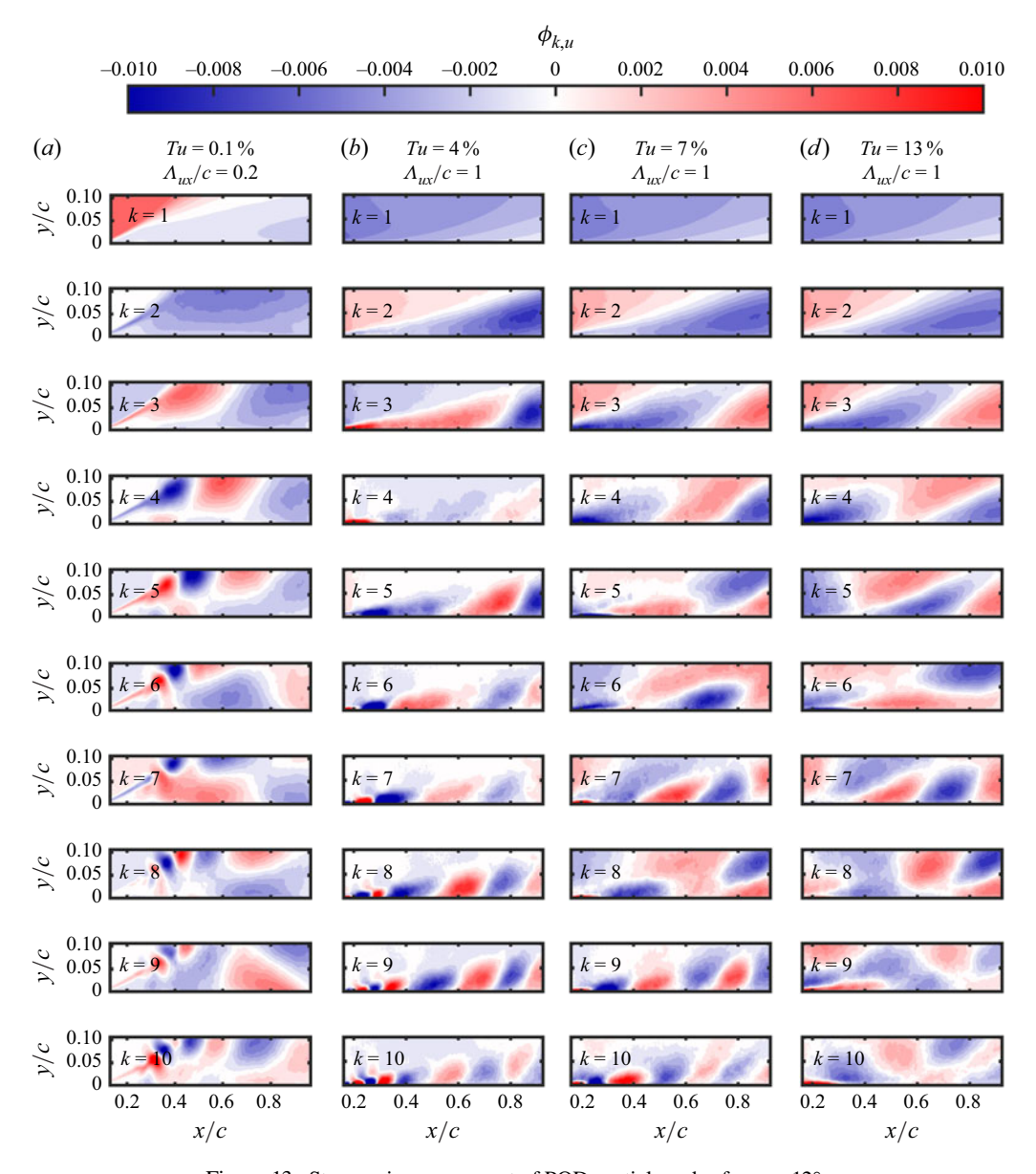


Figure 13. Streamwise component of POD spatial modes for $\alpha = 12^{\circ}$.

Tu = 7% (figure 12c) also displays spatially periodic structures in the boundary layer that are typical of vortex shedding from an LSB.

Mode 3 for Tu = 4% describes a large-scale change in the outer flow that is correlated to a streamwise elongated region within the boundary layer, suggestive of the streaky structures formed during bypass transition (Lengani & Simoni 2015). Like the second modes, the overall spatial structure of the third modes is also analogous for Tu = 4%, 7% and 13%, albeit reversed in sign. For Tu = 7% (figure 12c), the fourth mode also displays a relatively large wavelength change in the outer flow that is correlated to a streamwise elongated and inclined structure within the boundary layer. For Tu = 13% (figure 12d),

modes 5 and 8 also contain similar elongated and inclined structures that are expected to form during bypass transition (Nolan & Walsh 2012).

For the clean flow at $\alpha=12^\circ$ (figure 13a), the second mode is related to oscillations in the trajectory of the separated shear layer (e.g. Fang & Wang 2024). Similar to the clean flow at $\alpha=5^\circ$, the spatial POD modes for $\alpha=12^\circ$ are related to periodic vortex shedding from the separated shear layer at progressively smaller scales for $4 \le k \le 10$. For Tu=4% at $\alpha=12^\circ$ (figure 13b), modes 6–10 exhibit streamwise periodic structures in the boundary layer that are indicative of vortex shedding from an LSB located upstream of the field of view. The second spatial modes for Tu=4%, 7% and 13% at $\alpha=12^\circ$ are analogous and describe a large scale change in the streamwise velocity gradient of the outer flow, similar to the second modes for these levels of FSTI at $\alpha=5^\circ$. The third modes for elevated FSTI at $\alpha=12^\circ$ describe streamwise elongated and inclined structures suggestive of streaks.

The comparison of F-POD spatial modes pertaining to different flow conditions reveals how the FSTI affects the spatial structure of the most energetic coherent structures in the boundary layer. The relatively small-scale structures associated with shear layer vortex shedding are progressively relegated to lower relative energy content and structures with relatively longer streamwise length scales gain a greater portion of the overall turbulent kinetic energy as the FSTI is increased. The modes with longer streamwise length scales contain elongated oblique structures near the aerofoil surface, consistent with the streaks that are expected to form during bypass transition. However, the F-POD modes suggest that a thin LSB may persist to at least Tu = 7%, for which the signature of a spatially periodic vortex train is present near the wall in mode 10 at both angles of attack. The second F-POD modes for each of the cases of elevated FSTI describe a change in the streamwise pressure gradient. The relationship of the second modes to the streamwise pressure gradient will be used to infer changes in effective angle of attack in § 3.5.

The observation of relatively small-scale streamwise-periodic structures consistent with vortex shedding from the separated shear layer in the F-POD modes suggest that a thin LSB may form on the aerofoil at relatively high FSTIs in large-scale free stream turbulence. Spectral analysis was performed on the wall-normal velocity fluctuations at $y = \overline{\delta^*}$ to investigate the effect of large-scale high-intensity free stream turbulence on the characteristics of shear layer rollers, namely, their frequency, wavenumber and convection speed, since the characteristics of the shed vortices affect the ability of the separated shear layer to reattach (e.g. Marxen & Henningson 2011; Serna & Lazaro 2015). The wall-normal velocity fluctuations are chosen for the spectral analysis because they are more strongly correlated to the passage of shear layer roll-up vortices than the streamwise velocity fluctuations (e.g. Lengani et al. 2014). The wall-normal velocity fluctuations at $y = \delta^*$ form a two-dimensional dataset that is a function of time and streamwise location. For the clean flow at $\alpha = 12^{\circ}$ in the streamwise region where $y = \overline{\delta}^*$ is outside of the field of view, the wall-normal velocity fluctuation data were extracted at the upper edge of field of view. The power spectral density of the wall-normal fluctuating velocity component $(\mathcal{P}_{fk}(v'))$ is plotted in figure 14 versus frequency and wavenumber. The power spectral density was estimated by averaging the squared magnitude of the two-dimensional Fourier transform obtained using windows of 128 and 256 samples in the temporal and streamwise dimensions, respectively, with 50 % window overlap. This windowing procedure is a generalisation of the method of Welch (1967) to two-dimensional data. The presented power spectral density estimates are the result of averaging over a total of 460 windows: 2 windows in the streamwise dimension and 230 windows in the temporal dimension. The frequency resolution is $0.3\overline{u_{\infty}}/c$, the wavenumber resolution is 30/c and the relative uncertainty in power spectral density is less than 8 % (95 % confidence). The data are normalised using the mean boundary layer edge velocity $(\overline{u_e})$ at the upstream limit of the

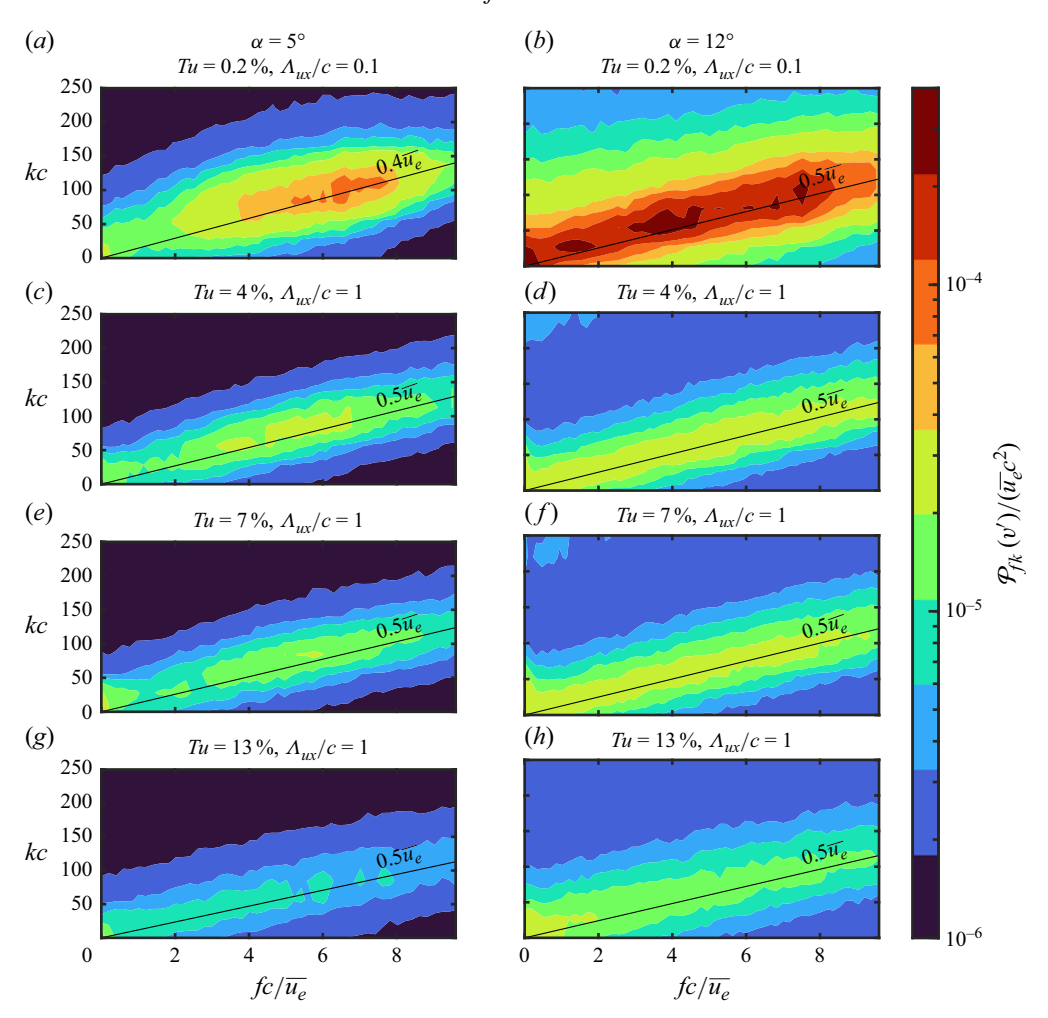


Figure 14. Frequency-wavenumber power spectral density of wall-normal velocity fluctuations at $y = \overline{\delta^*}$ for clean flow and elevated FSTI with $\Lambda_{ux}/c = 1$ at (a,c,e,g) $\alpha = 5^\circ$ and (b,d,f,h) $\alpha = 12^\circ$.

PIV field of view, which is near the location of boundary layer separation for those cases where there is an LSB or massively separated flow (figures 6 and 7).

At $\alpha=5^\circ$ (figure 14a), vortex shedding from the LSB in the clean flow produces a peak at $fc/\overline{u_e}=6.6$ ($fc/\overline{u_\infty}=9.8$) and kc=110, which is consistent with the fundamental frequencies and wavenumbers for vortex shedding from LSBs at similar chord Reynolds numbers (Toppings & Yarusevych 2023, 2024). The estimated wavenumber corresponds to a streamwise wavelength of 0.06c, which is in agreement with the streamwise wavelength of the stuctures near the location of maximum LSB height (x/c=0.49) in POD modes 6–10 for the clean flow (figure 12a). Relative to the clean flow, there is a reduction in the frequency, wavenumber and amplitude of the fundamental vortex shedding peak for the cases of elevated FSTI. The reduction in frequency and wavenumber of the vortex shedding peak is attributed to the reduction in the distance of the separated shear layer from the aerofoil surface, which is expected to reduce the frequency and wavenumber of the most amplified disturbances (e.g. Dovgal et al. 1994). The reduction in amplitude of the

vortex shedding peak is attributed to bypass transition, which leads to more rapid break-down of the spanwise roll-up vortices into three-dimensional turbulence (Hosseinverdi & Fasel 2019). Furthermore, the streaks formed due to free stream turbulence are expected to produce larger streamwise velocity fluctuations than wall-normal velocity fluctuations (e.g. Nolan & Walsh 2012), consistent with the fluctuating velocity statistics presented in figures 6 and 7. However, the discernible spectral peak of the wall-normal velocity fluctuations for Tu = 7% at $fc/\overline{u_e} = 5.7$ and kc = 84 (figure 14e) provides additional evidence that an LSB with periodic vortex shedding may persist at this FSTI.

At $\alpha=12^\circ$, there are relatively stronger and more broadband wall-normal velocity fluctuations in the clean flow (figure 14b) because the greater separation angle reduces the stability of the separated shear layer (e.g. Dovgal *et al.* 1994). Similar to the results from the lower angle of attack, increasing the FSTI at $\alpha=12^\circ$ also decreases the amplitudes of wall-normal velocity fluctuations. This is consistent with the more rapid breakdown of the roll-up vortices into three-dimensional turbulence at elevated FSTI observed in previous studies where bypass transition mechanisms become dominant (e.g. Hosseinverdi & Fasel 2019; Aniffa *et al.* 2023; Jaroslawski *et al.* 2023). The absence of a distinct spectral peak for the cases of elevated FSTI at $\alpha=12^\circ$ is attributed to the upstream movement of the vortex roll-up location relative to the PIV field of view at this angle of attack, with the consequence of earlier vortex breakdown and reduced coherence of wall-normal velocity fluctuations in the field of view.

In all of the spectra presented in figure 14, the amplitude of wall-normal velocity fluctuations is greatest along a convective ridge (e.g. Abraham & Keith 1996). The convective speed of these fluctuations, which is approximately equal to the vortex convection speed for cases where coherent vortex shedding occurs, was estimated from a linear fit to the highest amplitude wavenumber for each frequency. The uncertainty in convection speeds is estimated to be $0.1\overline{u_e}$ from the variations in convection speeds obtained with various window widths for the power spectral density estimation. At $\alpha = 5^{\circ}$, the convective speed is within $0.4 \le \overline{u_e} \le 0.5$, consistent with the convective speeds expected for shear layer roll-up vortices in LSBs (Yarusevych, Sullivan & Kawall 2009). At $\alpha = 12^{\circ}$, the convective speed remains at $0.5\overline{u_e}$ for both the clean flow condition, where the flow is massively separated, and for the attached flow conditions at elevated FSTI. Although the frequency content of wall-normal velocity fluctuations in the boundary layer becomes more broadband with increasing FSTI, the results of the frequency-wavenumber analysis suggest that the angle of attack and FSTI have a negligible effect on the convection speed of coherent structures formed in the transition process when normalised by the boundary layer edge velocity. The measured convection speeds are in agreement with the universal roll-up frequency scaling proposed by Yarusevych et al. (2009).

To illustrate the temporal variations in transition location that occur at elevated FSTI, the spatial entropy from the P-POD is plotted versus time and streamwise location in figures 15 and 16 for Tu = 0.1 %, 7 % and 13 % at $\alpha = 5^{\circ}$ and 12°, respectively. The entropy contours in these figures were obtained from time-resolved PIV measurements. All spatial entropy values below the transition threshold $(S_{s,P}/S_{g,t} < 1)$ are covered by the lowest contour level. The overall entropy of the entire velocity field at each moment in time is quantified by the spatial entropy computed from the F-POD $(S_{s,F})$, plotted as magenta lines in figures 15 and 16. Histograms of the instantaneous location of x_t from non-time-resolved data over a wider field of view are provided in the right column for each level of FSTI. The probabilities in the histograms are defined as the fraction of the time that the transition location is within each bin of width 0.025c.

In the clean flow at $\alpha = 5^{\circ}$ (figure 15a), there is a rapid increase in entropy at $x/c \approx 0.5$, corresponding to the onset of transition near the location of maximum LSB

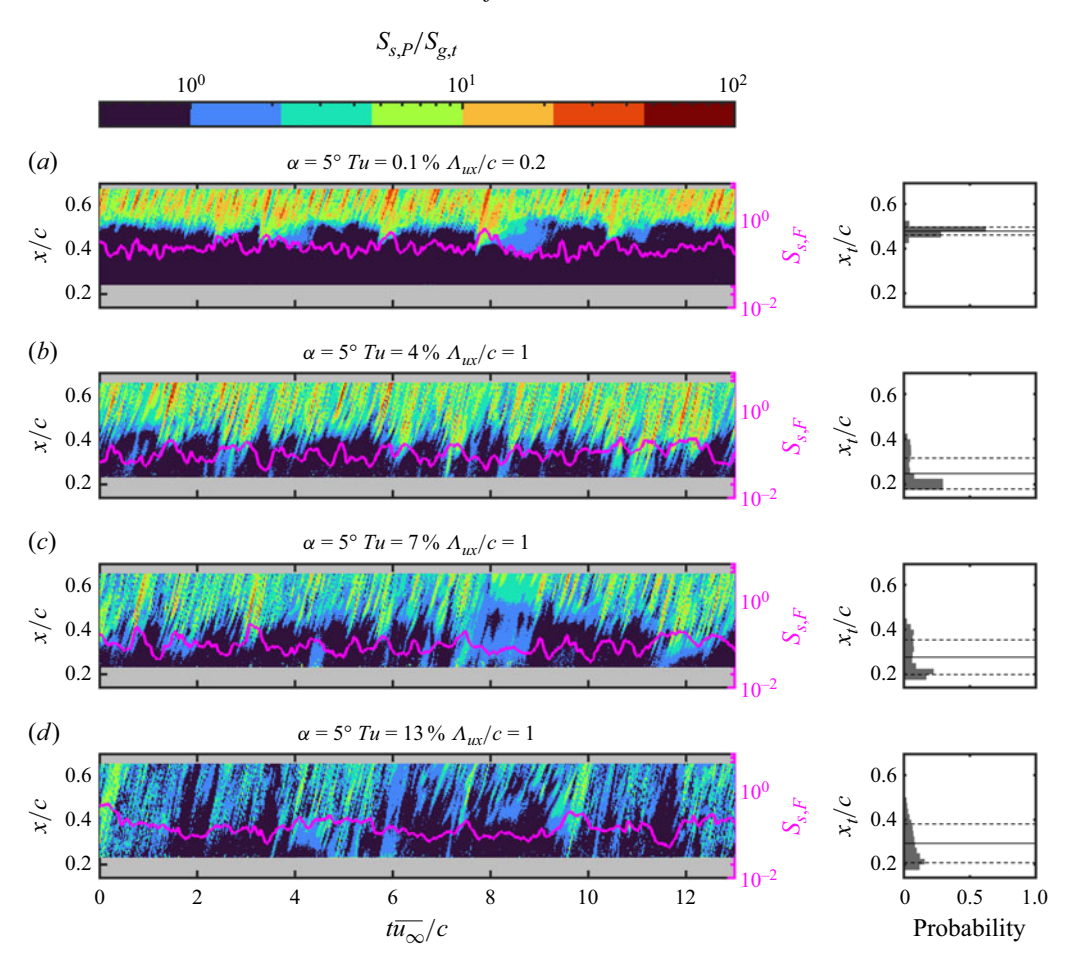


Figure 15. Left column shows contours of spatial entropy from P-POD at $\alpha = 5^{\circ}$. Grey areas are outside the PIV field of view. Magenta lines, spatial entropy from F-POD. Right column shows histograms of x_t . Solid lines, $\overline{x_t} \pm \sigma_{x_t}$.

thickness (figure 6a). For this case, the transition location determined from the entropy-based criterion remains relatively constant, with a mean of $\overline{x_t}/c = 0.48$ and a standard deviation of $\sigma_{x_t}/c = 0.02$, as shown in the histogram. The boundary layer consistently remains turbulent downstream of the mean reattachment location of the LSB (x/c = 0.6 figure 6a). Regions of the boundary layer with higher spatial disorder indicative of turbulent flow appear as oblique ridges of higher entropy. The slope of the ridges in the plot is proportional to their convective speed. The convective speed of the high-entropy ridges is approximately $0.4\overline{u_e}$ ($0.7\overline{u_\infty}$), which is consistent with the convective speed of the shear layer roll-up vortices estimated from the frequency wavenumber spectrum in figure 14. The consistency of the estimated convective speeds of the wall-normal velocity fluctuations and the spatial entropy fluctuations holds for varying flow conditions, confirming the suitability of spatial entropy as a spatio-temporally localised indicator of velocity field disturbances.

For $\alpha = 5^{\circ}$ with elevated FSTI (figures 15b and 15d), the mean streamwise location of transition is relatively unaffected by FSTI beyond Tu = 4%, but becomes more variable in time as the FSTI is increased. For example, for Tu = 13% (figure 15d) at

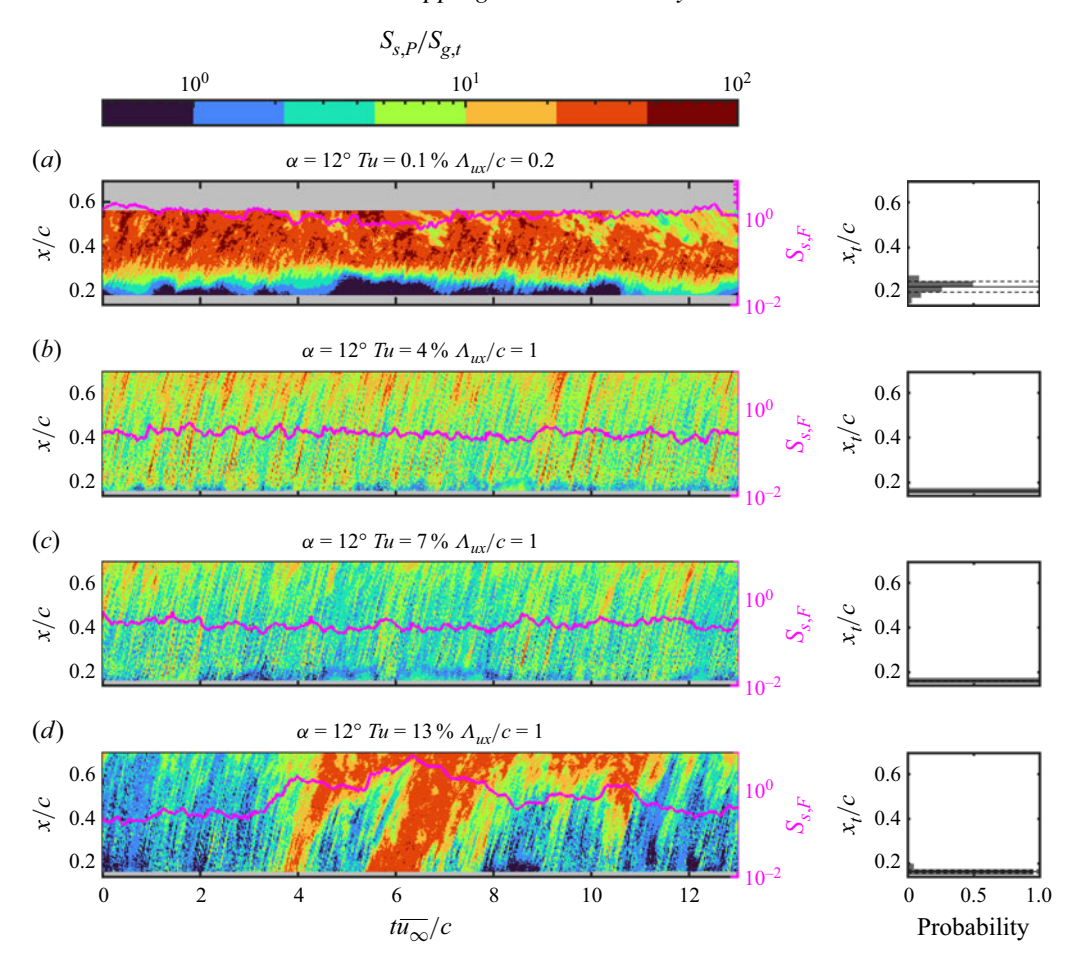


Figure 16. Left column shows contours of spatial entropy from P-POD at $\alpha = 12^{\circ}$. Grey areas are outside the PIV field of view. Magenta lines, spatial entropy from F-POD. Right column shows histograms of x_t . Solid lines, $\overline{x_t}$; dashed lines, $\overline{x_t} \pm \sigma_{x_t}$.

 $t\overline{u_{\infty}}/c = 9.5$, transition occurs upstream of the PIV field of view and at $t\overline{u_{\infty}}/c = 11.8$, laminar flow persists across the entire streamwise extent of the field of view. The mean measured transition locations for Tu = 4%, 7% and 13% are $\overline{x_t}/c = 0.25$, 0.28 and 0.30, respectively, and the standard deviations are $\sigma_{x_t}/c = 0.07$, 0.08 and 0.09, respectively.

The overall level of disorder in the flow over the entire field of view can be quantified by the spatial entropy obtained from the F-POD (magenta lines in figures 15 and 16). When the transition location moves upstream, the spatial entropy from the F-POD tends to increase. The spatial entropy from the F-POD will be used in § 3.5 to correlate overall changes in the disorder of the flow over the suction surface of the aerofoil to free stream velocity fluctuations upstream of the aerofoil.

Similar to the foregoing results for the clean flow at $\alpha = 5^{\circ}$, the transition location also remains relatively consistent for the clean flow at $\alpha = 12^{\circ}$ (figure 16). However, the separated shear layer transitions further upstream at the higher angle of attack because the more adverse pressure gradient causes earlier separation, which destabilises the shear layer (e.g. Diwan & Ramesh 2009). This is consistent with the earlier shear layer roll-up in figure 10(b). For Tu = 4% at $\alpha = 12^{\circ}$, transition frequently occurs sufficiently

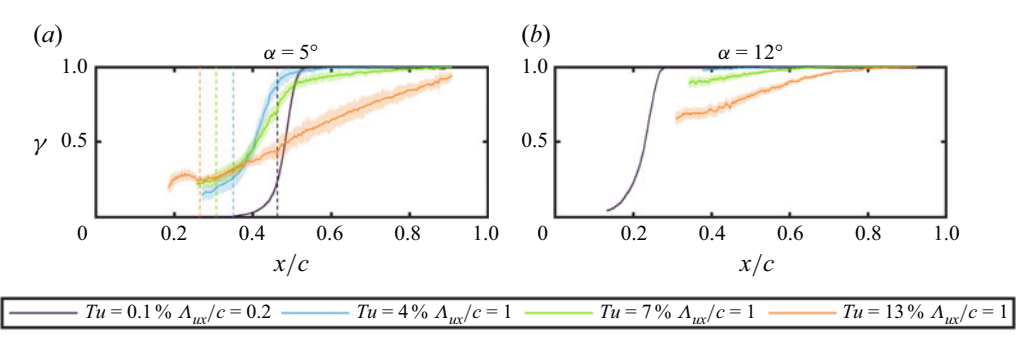


Figure 17. Intermittency factor for clean flow and elevated FSTI with $\Lambda_{ux}/c = 1$. Dashed lines, location of maximum shape factor. Shaded areas indicate uncertainty (95 % confidence).

upstream to prevent massive laminar separation from stalling the aerofoil (figure 16b). For all levels of elevated FSTI at $\alpha=12^\circ$ (figure 16b-d), the mean computed transition location is near the upstream limit of the field of view. Therefore, the standard deviations of the transition locations (dashed lines in figure 16) are likely underestimated. For the cases of Tu=4% and 7% (figures 16b and 16c), the computed transition location is upstream of x/c=0.175 for more than 98 % of the measurement period. Intermittent periods of reduced spatial entropy indicative of laminar flow still occur in the attached boundary layer at $\alpha=12^\circ$, notably at Tu=13% (figure 16d). However, the spatial and temporal extent of these laminar periods are substantially reduced compared with those for elevated FSTI at $\alpha=5^\circ$. For Tu=13% at $\alpha=12^\circ$, there are also notable intermittent periods of substantially increased spatial entropy. It will be shown later that these periods are related to intermittent massive separation of the suction surface boundary layer.

Using the spatial entropy from the P-POD $(S_{s,P})$ and the transition thresholds $(S_{g,t})$, the intermittency factor (γ) can be calculated. The intermittency factor is defined as the fraction of time that $S_{s,P} > S_{g,t}$ and thus indicates the probability that the flow is turbulent at a given streamwise location (e.g. Hedley & Keffer 1974). The intermittency factor is plotted in figure 17 for locations downstream of the minimum global entropy. The locations of maximum shape factor at $\alpha = 5^{\circ}$ used to define the transition thresholds are indicated by the dashed lines in figure 17(a). For all levels of FSTI at $\alpha = 5^{\circ}$, $\gamma \approx 0.25$ at the location of maximum shape factor. In the clean flow at both $\alpha = 5^{\circ}$ and 12°, the intermittency factor rapidly increases from $\gamma \approx 0$ to $\gamma \approx 1$ over a distance of approximately 0.15c. The reduction in intermittency factor for elevated FSTI relative to the clean flow for x/c > 0.5 at $\alpha = 5^{\circ}$ is consistent with the increased variability in transition location and intermittent periods of laminar flow for elevated FSTI in figure 15. For x/c < 0.8at $\alpha = 12^{\circ}$ (figure 17b), there is a decrease in intermittency factor with increasing FSTI, consistent with the larger variations in spatial entropy with increasing FSTI in figure 16. Overall, as the FSTI is increased, the maximum rate of change of the intermittency factor becomes more gradual, indicating a higher probability of laminar flow persisting downstream of the mean transition location.

To characterise the frequencies associated with the large variations in transition location observed for $\alpha = 5^{\circ}$, the power spectral density of the spatial entropy fluctuations from the P-POD ($\mathcal{P}_f(S'_{s,P})$) performed on the non-time-resolved PIV measurements for $\alpha = 5^{\circ}$ are presented in figure 18(a, b) for $\Lambda_{ux}/c = 1$ and 2, respectively. The spectra presented in figure 18 were obtained after averaging the spectra over 0.4 < x/c < 0.5, where relatively large amplitude and low-frequency variations in spatial entropy occur for all levels of FSTI

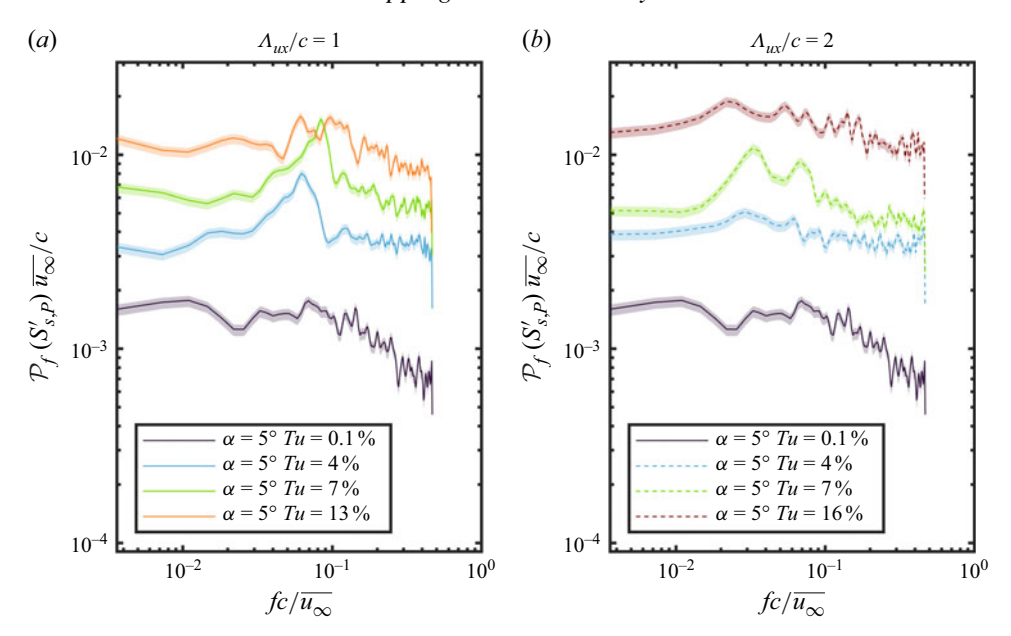


Figure 18. Power spectral density of spatial entropy fluctuations from P-POD averaged over 0.4 < x/c < 0.5 for $\alpha = 5^{\circ}$.

tested (figure 15). The clean flow with $\Lambda_{ux}/c = 0.2$ is shown in both plots for reference. The spectra were obtained using Welch's method with a Hamming window of length 128 samples and 50 % window overlap, yielding a frequency resolution of 0.007 Hz.

In the clean flow, the transition location is relatively steady and there are no substantial peaks in the spatial entropy spectrum. For increasing FSTI, there is an increase in the amplitudes of spatial entropy fluctuations, consistent with the low-frequency variability in the transition location observed for high FSTI (figure 15). For Tu = 4% and 7%, increasing the integral length scale from $\Lambda_{ux}/c=1$ to 2 has the effect of shifting the largest amplitude fluctuations to lower frequencies. For $\Lambda_{ux}/c=1$, there are prominent peaks at $fc/u_{\infty} = 0.06$ and 0.08 for Tu = 4% and 7%, respectively (figure 18a). These peaks are consistent with the frequencies of the largest amplitude free stream velocity fluctuations for these conditions (cf. figure 3). For $\Lambda_{ux}/c = 2$, the frequencies of the largest amplitude spatial entropy fluctuations are reduced to $fc/u_{\infty} = 0.03$ for both Tu = 4% and 7 % (figure 18b), consistent with the reduction in frequency of the largest amplitude free stream velocity fluctuations. There is also a reduction in the frequency of the largest amplitude spatial entropy fluctuations for the case of Tu = 16%, $\Lambda_{ux} = 2$ relative to Tu = 13 %, $\Lambda_{ux} = 1$. Considering that the change of integral length scale had a negligible influence on the mean flow, these results suggest that variations in Λ_{ux} , when $\Lambda_{ux} \sim c$, do not directly affect transition through the receptivity process. Instead, when $\Lambda_{ux} \sim c$, changes in Λ_{ux} influence the frequency at which variations of the global flow development occur about the mean.

The relationship between the flow field development and the spatial entropy computed from the F-POD (lines in figure 15, 16) is demonstrated in figure 19, which presents instantaneous contours of streamwise velocity for the PIV snapshots of the 1st percentile of $S_{s,F}$ (figure 19a,b) and the 99th percentile (figure 19c,d) of $S_{s,F}$ at Tu = 13%. Recall, the value of $S_{s,F}$ computed from the F-POD quantifies the spatial disorder in the flow over the entire field of view. In the PIV snapshots of the 1st percentile of $S_{s,F}$, the

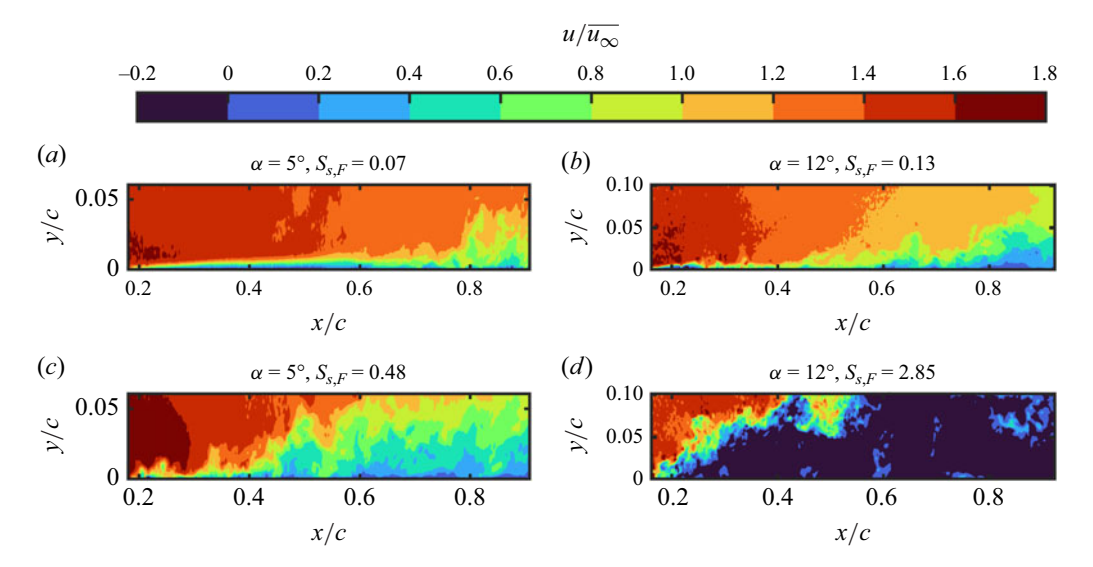


Figure 19. Instantaneous streamwise velocity measurements for the (a,b) 1st percentile of $S_{s,F}$ and (c,d) 99th percentile of $S_{s,F}$ from the F-POD observed at (a,c) $\alpha=5^{\circ}$ and (b,d) $\alpha=12^{\circ}$ for Tu=13% and $\Lambda_{ux}/c=1$.

boundary layer remains thin and laminar over a substantial portion of the field of view. For the snapshots of the 99th percentile of $S_{s,F}$, the boundary layer is relatively thicker and at $\alpha = 12^{\circ}$, reverse flow covers a substantial portion of the field of view. Figure 19(*d*) confirms that the periods of relatively higher spatial entropy for $\alpha = 12^{\circ}$ and Tu = 13% in figure 16(*d*) are associated with intermittent massive separation from the aerofoil surface. It is likely that these periods of massive separation are partly responsible for the measured reduction in time-averaged lift coefficient for Tu = 13% and 16% relative to Tu = 4% and 7% at $\alpha = 12^{\circ}$ (figure 4).

3.5. Correlation of oncoming disturbances to boundary layer development

Measurements from the hotwire anemometer placed 10c upstream of the aerofoil and synchronised with the PIV system are used to explore the relationship of the oncoming velocity magnitude to the flow over the suction surface of the aerofoil. The correlation coefficient between the velocity magnitude measured by the hotwire and the mean streamwise velocity averaged over the PIV field of view ($\langle u \rangle$) is plotted in figure 20(a,b) versus time lag for $\alpha = 5^{\circ}$ and 12° , respectively. Data were used from the PIV measurements at 100 Hz for better statistical convergence at the expense of temporal resolution. The results show a positive peak at $t\overline{u_{\infty}}/c \approx 10$ for all levels of elevated FSTI at both $\alpha = 5^{\circ}$ and 12°. Since the hotwire was positioned a distance of 10c upstream of the quarter-chord of the aerofoil, this peak corresponds to disturbances in the oncoming flow that convect at the free stream velocity and are sufficiently large to maintain their temporal coherence over that distance. The negative correlation peaks that occur at $tu_{\infty}/c\approx 5$ and 15 are attributed to inevitable opposite-sign changes of incoming flow velocity preceding and following that responsible for the dominant correlation peak. For example, due to the requirement for continuity, a significant, large-scale increase in free stream velocity must be preceded or followed by a decrease in free stream velocity to maintain the overall average flow rate through the test section.

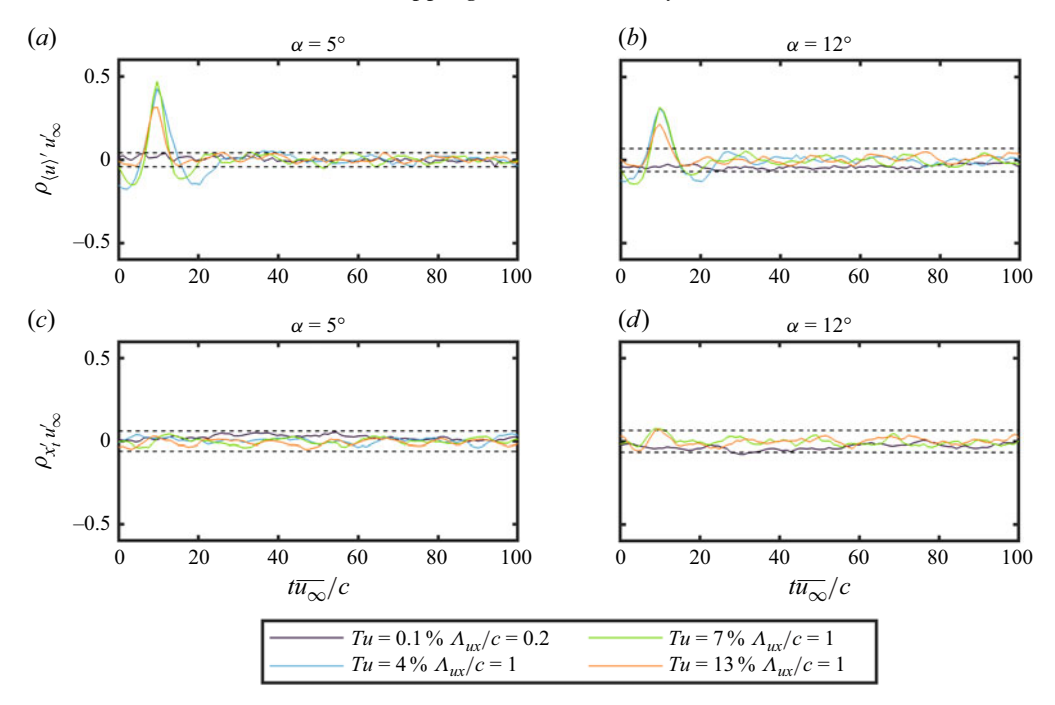


Figure 20. (a, b) Correlation coefficient between upstream hotwire anemometer velocity and spatially averaged streamwise velocity from side-view PIV and (c,d) transition location from P-POD. Values outside the dashed lines are significant at a 95 % confidence level.

Because of the closed test section, the active grid also produces pressure waves that likely affect the boundary layer development on the aerofoil (e.g. Collins & Zelenevitz 1975). The time lag for a pressure wave to propagate from the hotwire to the aerofoil is $t\overline{u_\infty}/c\approx 0.003$. Although the influence of such pressure waves on the aerofoil boundary layer cannot be discounted, the convective correlation peaks at $t\overline{u_\infty}/c\approx 10$ are substantially larger in magnitude than the correlations for $t\overline{u_\infty}/c\approx 0.003$. This suggests that convective vortical structures in the oncoming flow are primarily responsible for the variations in boundary layer development on the suction surface of the aerofoil. In the clean flow, there are no significant correlations between the oncoming flow velocity magnitude and the spatially averaged velocity magnitude of the PIV measurements due to the order of magnitude lower FSTI.

The correlation coefficients between the upstream velocity magnitude and the transition location determined using the entropy-based method from the P-POD (§ 3.3.1) are presented in figures 20(c) and 20(d). Note that, for the case of Tu = 4% at $\alpha = 12^{\circ}$, no correlation coefficient could be computed because the transition location was always upstream of the side-view PIV field of view. The correlations are largely insignificant for all time lags at a 95% confidence level. Furthermore, no statistically significant correlations between the oncoming velocity magnitude and the turbulent kinetic energy within the boundary layer were found when the velocity fluctuations were normalised by the spatially averaged velocity within the boundary layer to account for the expected increase in turbulent kinetic energy with increasing free stream velocity. Thus, it is unlikely that large-scale fluctuations in effective oncoming velocity magnitude are responsible for the intermittent periods of expedited and delayed transition observed at high FSTI.

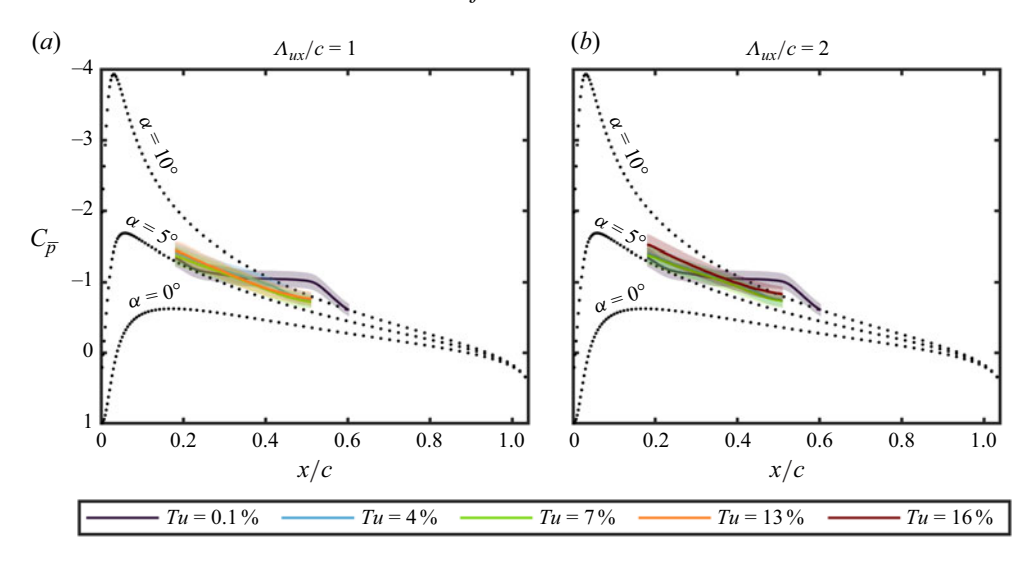


Figure 21. Estimated mean surface pressure distributions at $\alpha = 5^{\circ}$. Shaded areas denote uncertainty (95 % confidence). Dotted lines, inviscid surface pressure distributions from XFOIL (Drela 1989).

In addition to fluctuations in the free stream velocity magnitude, large-scale free stream turbulence also leads to fluctuations in effective angle of attack, which may influence the boundary layer transition process on the aerofoil (e.g. Herbst *et al.* 2018; Kay *et al.* 2020). The variations in effective angle of attack due to fluctuations in free stream velocity direction were characterised from estimated variations in the suction surface pressure coefficients. The estimations were performed for $\alpha = 5^{\circ}$, where the boundary layer remains relatively thin and massive separation is unlikely to occur. The instantaneous surface pressure coefficient at a given x location was estimated from the local instantaneous boundary layer edge velocity as $C_p = 1 - (u_e/\overline{u_{\infty}})^2$, assuming that the wall-normal pressure gradient may be neglected within the boundary layer (e.g. Diwan & Ramesh 2012). The free stream velocity used for calculating the pressure coefficients was the mean free stream velocity $(\overline{u_{\infty}})$ obtained from a calibration of the pressure drop across the wind tunnel contraction upstream of the active grid.

The mean surface pressure coefficient distributions for $\alpha=5^\circ$ are plotted in figure 21, along with inviscid surface pressure distributions for angles of attack of $\alpha=0^\circ$, 5° and 10° computed using the XFOIL software (Drela 1989). The mean surface pressure coefficients for the clean flow with $A_{ux}/c=0.2$ are plotted in both figures 21(a) and 21(b) for reference. The maximum uncertainty in the estimated mean pressure coefficients is less than 0.2. In the clean flow, the $C_{\overline{p}}$ distribution initially follows the inviscid distribution at the geometric angle of attack of $\alpha=5^\circ$, before diverging near the boundary layer separation point and plateauing. A relatively rapid pressure recovery occurs between the location of maximum LSB thickness and the mean reattachment point, consistent with the surface pressure distribution expected of a short LSB (Horton 1968). For elevated FSTI, the pressure plateau is suppressed and the pressure distributions follow that for the inviscid flow at $\alpha=5^\circ$ more closely, consistent with the thinning of the LSB. However, there is still an increase in suction relative to the inviscid flow for Tu=4% and 7%, suggesting that an LSB persists.

Previously, it was shown that the second POD mode for the cases of elevated FSTI was related to the streamwise pressure gradient. Since increases in effective angle of attack are expected to lead to a more adverse streamwise pressure gradient, variations in the

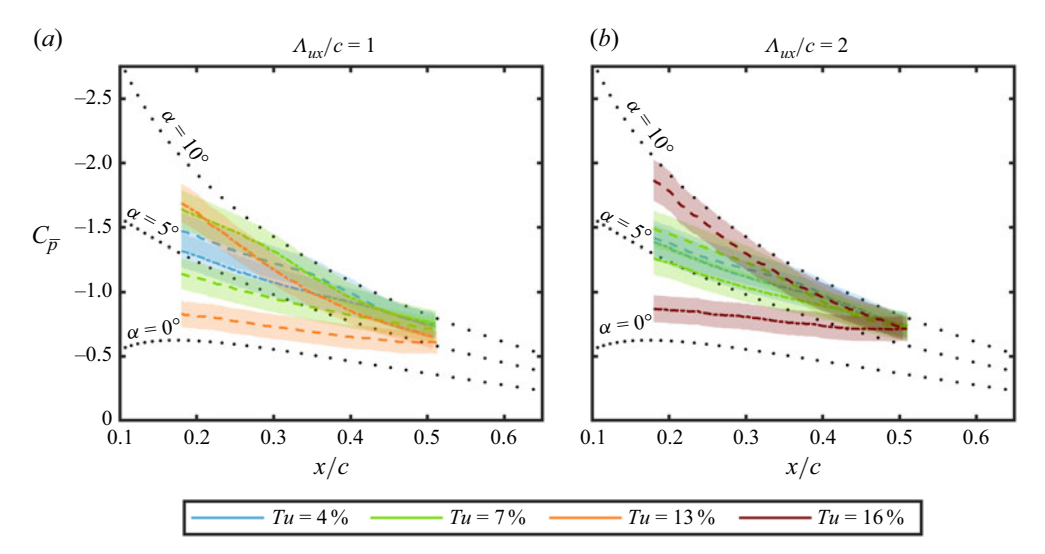


Figure 22. Estimated conditional surface pressure distributions at $\alpha = 5^{\circ}$. Dashed lines, conditional average of $a_2 < \overline{a_2} - \sigma_{a_2}$; dash-dotted lines, conditional average of $a_2 > \overline{a_2} + \sigma_{a_2}$; dotted lines, inviscid surface pressure distributions from XFOIL (Drela 1989).

effective angle of attack at elevated FSTI were characterised using conditional averaging of the estimated pressure coefficient distributions based on the temporal coefficient of the second POD mode. The surface pressure distributions of the conditional averages of snapshots for a_2 falling below or above the mean value by more than one standard deviation are plotted in figure 22 as dashed and dash-dotted lines, respectively, for the cases of elevated FSTI. Depending on the sign of the second spatial POD mode (figure 12), the $C_{\overline{p}}$ distributions conditioned on $a_2 < \overline{a_2} - \sigma_{a_2}$ and $a_2 > \overline{a_2} + \sigma_{a_2}$ show either a decrease or increase in pressure gradient consistent with a change in effective angle of attack. For Tu = 13% (figure 22a) and Tu = 16% (figure 22b), the conditional pressure distributions begin to approach the inviscid pressure distributions for $\alpha = 10^{\circ}$ and $\alpha = 0^{\circ}$. The pressure gradients of the conditional averages for Tu = 16% are consistent with changes in effective angle of attack of nearly $\pm 5^{\circ}$ relative to the aerofoil's fixed geometric angle of attack of $\alpha = 5^{\circ}$. This range of effective angle of attack variation is in reasonable agreement with the results of Kay et al. (2020), who reported standard deviations of the effective angle of attack of 2.4° and 6.9° for Tu = 5% and 15%, respectively. For Tu = 4% and 7%, the variations in effective angle of attack in the present study are more difficult to estimate from a comparison with inviscid surface pressure distributions due to the increase in suction caused by the relatively larger LSB forming at these FSTIs. However, the conditional surface pressure distributions from these cases are consistent with the expected increase in effective angle of attack variation with increasing FSTI. Note that the differences in the surface pressure distributions for $\Lambda_{ux}/c=1$ and 2 at constant FSTI (Tu = 4% and 7%) are within the experimental uncertainty. This finding implies changes in Λ_{ux} , when Λ_{ux} remains of the order of the aerofoil chord, do not substantially affect the effective angle of attack variations experienced by the aerofoil.

Figure 22 demonstrates that substantial changes in pressure gradient occur at high FSTI that are likely associated with changes in effective angle of attack. When the second POD mode for the cases of elevated FSTI is related to a large-scale change in the edge velocity

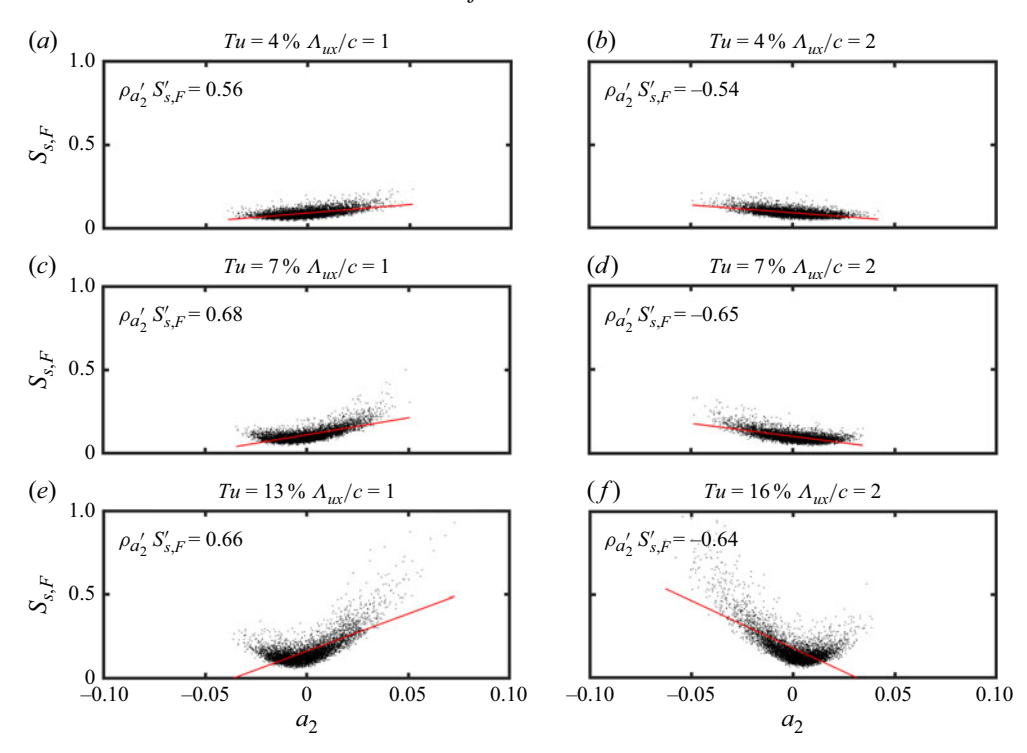


Figure 23. Correlation between the temporal coefficient of the second mode a_2 and spatial entropy $S_{s,F}$ from F-POD. Red lines show best linear fit.

gradient (cf. figures 12 and 13) and therefore to a large-scale change in surface pressure distribution, the temporal coefficient of the second POD mode (a_2) is expected to be correlated to the spatial entropy from the F-POD. This is because stronger adverse pressure gradients lead to earlier boundary layer transition (Dellacasagrande et al. 2020), causing an increase in disorder within the flow field. The relationship between a_2 and the spatial entropy from the F-POD is shown in figure 23 for the cases of elevated FSTI. If the degree of disorder within the flow field was independent of the second POD mode, the distribution of the data points in each scatter plot would have reflective symmetry about $a_2 = 0$. In all cases, the scatter plots are visibly asymmetric about $a_2 = 0$, and the correlations between a_2 and $S_{s,P}$ are significant at a 95 % confidence level as verified by statistical P-value evaluation. The sign of the correlation coefficients $(\rho_{a_2S_{s,F}})$ vary according to the sign of the spatial modes, but are all consistent with increasing spatial entropy with increasing adverse pressure gradient when accounting for the sign of the spatial modes (cf. figure 12 for $\Lambda_{ux}/c=1$). Weaker but still statistically significant correlations were found directly between a_2 and x_t , consistent with the tendency for earlier transition during periods of stronger adverse pressure gradient. Thus, the observed correlations between a_2 and the spatial entropy suggest that the variations in effective angle of attack caused by large-scale free stream turbulence are linked to the relatively large variations in transition location and boundary layer thickness observed at high FSTI.

The prevalent effect of angle of attack fluctuations compared with that of the velocity magnitude is consistent with the much higher sensitivity of the transition process to comparable relative changes in angle of attack than chord Reynolds number for quasisteady conditions (Boutilier & Yarusevych 2012b; Park, Shim & Lee 2020). For example,

the data of Boutilier & Yarusevych (2012b) indicate that for a NACA 0018 aerofoil operating at $Re_c=1\times 10^5$ and $\alpha=5^\circ$, a 50% increase in Re_c would cause a 0.05c upstream movement in transition location, compared with a 0.1c upstream movement for a 50% increase in angle of attack. Furthermore, the inferred relative fluctuations in angle of attack at high FSTI are substantially higher than those in chord Reynolds number. For example, at Tu=16%, $\Lambda_{ux}/c=2$, the relative fluctuations in effective chord Reynolds number are of the order of 10%. In contrast, an order of $0.1\overline{u_\infty}$ fluctuations in vertical velocity component correspond to approximately arctan $(0.1)\approx 6^\circ$ fluctuations in the angle of attack (i.e. $\sim 100\%$ of the geometric angle of attack). Thus, the relative fluctuations in angle of attack are an order of magnitude higher than those in Reynolds number for this test case.

4. Concluding remarks

Wind tunnel tests were performed on a NACA 0018 aerofoil model operating at a chord Reynolds number of $Re_c = 7.0 \times 10^4$. Free stream turbulence was generated using an active turbulence grid at intensities of up to Tu = 16%. The integral length scale of the elevated free stream turbulence was fixed at $\Lambda_{ux}/c = 1$ and 2. The mean aerodynamic loads on the aerofoil were measured using a force balance, and the velocity field at the midspan of the aerofoil on the suction surface was measured using two-component PIV at angles of attack of $\alpha = 5^{\circ}$ and 12° .

A laminar separation bubble formed on the aerofoil in the clean flow at $\alpha = 5^{\circ}$. The LSB became thinner as the FSTI was increased. Although mean reverse flow was not detected for Tu = 7 %, LSB formation likely persisted at this level of FSTI since a local maximum of the shape factor occurred in the vicinity of the mean transition location. Evidence of this LSB was also seen in the mean and fluctuating velocity fields, which exhibited features consistent with those observed in the reattachment region of the LSB in the clean flow. Furthermore, a spectral peak consistent with vortex shedding from the separated shear layer was observed in the wall-normal velocity fluctuations for Tu = 7%. At Tu = 13%, the FSTI was sufficiently high that these features of LSB formation were no longer seen. However, a local maximum in the shape factor persisted at Tu = 13%. The spatial POD modes of the measured velocity fields indicated that the most energetic coherent structures in the clean flow were those formed from roll-up of the separated shear layer. With increasing FSTI, the modes related to shear layer roll-up vortices were progressively superseded in relative energy content by modes containing structures with relatively larger streamwise length scales. These modes showed similarity with elongated streaks typical of bypass transition and relatively large-scale modulations of the outer flow velocity.

At $\alpha=12^\circ$, the aerofoil was stalled in the clean flow. Increasing the FSTI caused the separated shear layer to reattach, leading to the formation of an LSB with measurable reverse flow. Due to the stronger adverse pressure gradient at the higher angle of attack, the LSB formed sufficiently far upstream that it was not completely eliminated by bypass transition, and evidence of LSB formation at Tu=13% was found in the mean and fluctuating velocity fields for $\alpha=12^\circ$. The persistence of the LSB at an FSTI of Tu=13% is notable because this FSTI is substantially higher than the levels of FSTI whose effects on LSBs have been studied previously (e.g. Simoni *et al.* 2017; Istvan & Yarusevych 2018; Dellacasagrande *et al.* 2020; Jaroslawski *et al.* 2023).

Consistent with prior studies of the effects of free stream turbulence on aerofoil performance at aerodynamically low Reynolds numbers (e.g. Cao *et al.* 2011; Mahallati *et al.* 2012; Istvan *et al.* 2018; Li & Hearst 2021), elevated free stream turbulence increased

the stall angle and maximum lift coefficient relative to the clean flow because of an advancement of the mean boundary layer transition location. At moderate angles of attack, free stream turbulence decreased the lift coefficient relative to the clean flow due to suppression of the suction surface LSB.

Despite the expected and observed upstream advancement of the mean boundary layer transition location with increasing FSTI, at the large integral length scales ($\Lambda_{ux} \sim c$) considered in this study, increasing the FSTI caused notable intermittent periods of substantially delayed transition at $\alpha = 5^{\circ}$. In some of these periods, the boundary layer remained laminar over a majority of the suction surface. This observation highlights the importance of both the intensity and length scale of free stream turbulence on the boundary layer development. The spatial entropy of the POD modes of measured velocity profiles was used to identify the instantaneous location of boundary layer transition. The variations in instantaneous transition location became greater as the FSTI was increased, leading to a reduction in the slope of the intermittency factor. Although the mean flow was attached to the suction surface for elevated FSTI at $\alpha = 12^{\circ}$, periods of intermittent massive separation were observed to occur for Tu = 13% at this angle of attack. At both angles of attack investigated with PIV measurements, the spatial entropy of the entire field of view was demonstrated to provide an indication of the spatial extent of turbulent flow.

A correlation between the observed instantaneous variations in the boundary layer development and oncoming velocity magnitude fluctuations in the free stream was investigated. However, no significant correlation was found between large-scale variations in oncoming velocity magnitude and the boundary layer transition process. In contrast, variations in the spatial extent of turbulence in the boundary layer were linked to changes in effective angle of attack caused by oncoming large-scale coherent structures. This was demonstrated through the correlation between the temporal coefficient of the second POD mode, which described the streamwise pressure gradient, and the spatial entropy of the velocity field. Increases in the streamwise adverse pressure gradient, expected to occur during increases in effective angle of attack, were correlated with higher spatial entropy, indicating earlier transition. Thus, large-scale fluctuations in effective angle of attack likely cause substantial variations of the transition location on the suction surface of the aerofoil when $A_{ux} \sim c$. By comparing the surface pressure coefficient distributions estimated from PIV measurements to those calculated for inviscid flow, it was estimated that the effective angle of attack undergoes fluctuations with an amplitude approaching 5° at the highest levels of FSTI tested. These fluctuations in effective angle of attack lead to intermittent massive separation at pre-stall angles of attack, which reduces aerofoil performance relative to lower FSTIs.

Changing the integral length scale from $\Lambda_{ux}/c=1$ to 2 had a negligible effect on the mean flow fields, the lift and drag coefficients, and the magnitude of the variations in effective angle of attack. This is in contrast with previous studies at smaller integral length scales ($\Lambda_{ux} \sim 0.1c$), which have reported measurable changes in pre-stall aerodynamic performance (Cao *et al.* 2011) and boundary layer disturbance growth rates (Jaroslawski *et al.* 2023) with relatively small changes in integral length scale. This suggests that the transition process is more sensitive to changes in integral length scale when $\Lambda_{ux} \ll c$, but is less so when $\Lambda_{ux} \sim c$. However, in the present experiments, changing the integral length scale changed the frequency at which variations about the mean flow occurred. Thus, incoming flow disturbances with characteristic lengths of the order of the aerofoil chord do not directly affect boundary layer transition through the receptivity process, but rather through variations in global aerofoil operating conditions.

Supplementary movie. Supplementary movie is available at https://doi.org/10.1017/jfm.2025.10747.

Sampling frequency	3.9 kHz			
Angle of attack	$\alpha = 5^{\circ}$		$\alpha = 12^{\circ}$	
Active turbulence grid	No	Yes	No	Yes
Cropped sensor size	$2175 \text{ px} \times 351 \text{ px}$	$1916 \text{px} \times 415 \text{px}$	$1791 \text{ px} \times 415 \text{ px}$	$2431 \text{ px} \times 351 \text{ px}$
Field of view	$0.74c \times 0.09c$	$0.43c \times 0.06c$	$0.40c \times 0.07c$	$0.55c \times 0.06c$
Sampling time	3.79 s	3.79 s	3.90 s	3.39 s

Table 3. PIV fields of view and sampling times for time-resolved measurements.

Sampling frequency	0.1 kHz			
Angle of attack	$lpha=5^{\circ}$		$\alpha = 12^{\circ}$	
Active turbulence grid	No	Yes	No	Yes
Cropped sensor size	$3327 \mathrm{px} \times 607 \mathrm{px}$	3301 px × 575 px	$3967 \text{px} \times 799 \text{px}$	$3967 \text{px} \times 799 \text{px}$
Field of view	$0.73c \times 0.09c$	$0.75c \times 0.06c$	$0.88c \times 0.11c$	$0.90c \times 0.11c$
Sampling time	55.98 s	59.09 s	35.68 s	35.68 s

Table 4. PIV fields of view and sampling times for non-time-resolved measurements.

Acknowledgements. The authors thank Mr Florian Kähler for designing the active turbulence grid, Mr Jason Benninger for manufacturing the aerofoil model and Dr Christopher Morton for lending the PIV camera.

Funding. The authors acknowledge the support of the Natural Sciences and Engineering Research Council of Canada (NSERC).

Declaration of interests. The authors report no conflict of interest.

Author contributions. C. Toppings: Conceptualisation, Methodology, Software, Formal analysis, Investigation, Data curation, Writing - original draft, Writing - review & editing, Visualisation. S. Yarusevych: Conceptualisation, Methodology, Formal analysis, Resources, Data curation, Writing - review & editing, Visualisation, Supervision, Project administration, Funding acquisition.

Appendix

The PIV camera fields of view and sampling times for time-resolved measurements and non-time-resolved measurements are tabulated in tables 3 and 4, respectively.

REFERENCES

ABDELSAMIE, A., JANIGA, G. & THÉVENIN, D. 2017 Spectral entropy as a flow state indicator. *Intl J. Heat Fluid Flow* **68**, 102–113.

ABRAHAM, B.M. & KEITH, W.L. 1996 Direct measurements of turbulent boundary layer wall pressure wavenumber - frequency spectra. In *ASME International Mechanical Engineering Congress and Exposition, Proceedings (IMECE) 1996-V (March)*, pp. 177–187. American Society of Mechanical Engineers.

ANIFFA, M., CAESAR, V.S., DABARIA, V. & MANDAL, A.C. 2023 Characteristics of geometry-and pressure-induced laminar separation bubbles at an enhanced level of free-stream turbulence. *J. Fluid Mech.* 957, A19.

AUBRY, N., GUYONNET, R. & LIMA, R. 1991 Spatiotemporal analysis of complex signals: theory and applications. *J. Stat. Phys.* **64** (3–4), 683–739.

BOUTILIER, M.S.H. & YARUSEVYCH, S. 2012a Effects of end Plates and blockage on low-Reynolds-number flows over airfoils. AIAA J. 50 (7), 1547–1559.

BOUTILIER, M.S.H. & YARUSEVYCH, S. 2012b Parametric study of separation and transition characteristics over an airfoil at low Reynolds numbers. *Exp. Fluids* **52** (6), 1491–1506.

- BOUTILIER, M.S.H. & YARUSEVYCH, S. 2012c Separated shear layer transition over an airfoil at a low Reynolds number. *Phys. Fluids* **24** (8), 084105.
- BURGMANN, S. & SCHRÖDER, W. 2008 Investigation of the vortex induced unsteadiness of a separation bubble via time-resolved and scanning PIV measurements. *Exp. Fluids* **45** (4), 675–691.
- CANEPA, E., CRIVELLINI, A., DELLACASAGRANDE, M., GHIDONI, A. & NOVENTA, G. 2025 The effect of streaks on the breakup of Kelvin–Helmholtz rolls in a geometry-induced laminar separation bubble. *Phys. Fluids* 37, 084109.
- CAO, N., TING, D.S.-K. & CARRIVEAU, R. 2011 The performance of a high-lift airfoil in turbulent wind. Wind Engng 35 (2), 179–196.
- CARMICHAEL, B.H. 1981 Low reynolds number airfoil survey. Tech. Rep. NASA CR-165803. Low Energy Transportation Systems.
- CHATTERJEE, A. 2000 An introduction to the proper orthogonal decomposition. Curr. Sci. 78 (7), 808-817.
- CHEN, H., REUSS, D.L. & SICK, V. 2012 On the use and interpretation of proper orthogonal decomposition of in-cylinder engine flows. *Meas. Sci. Technol.* 23, 085302.
- COLLINS, F.G. & ZELENEVITZ, J. 1975 Influence of sound upon separated flow over wings. AIAA J. 13 (3), 408–410.
- COULL, J.D. & HODSON, H.P. 2011 Unsteady boundary-layer transition in low-pressure turbines. J. Fluid Mech. 681 (1), 370–410.
- DAMIOLA, L., SIDDIQUI, M.F., RUNACRES, M.C., DE TROYER, T. 2023 Influence of free-stream turbulence intensity on static and dynamic stall of a NACA 0018 aerofoil. *J. Wind Engng Ind. Aerodyn.* 232, 105270.
- DELLACASAGRANDE, M., BARSI, D., LENGANI, D., SIMONI, D. & VERDOYA, J. 2020 Response of a flat plate laminar separation bubble to Reynolds number, free-stream turbulence and adverse pressure gradient variation. Exp. Fluids 61 (6), 128.
- DELNERO, J.S., MARAÑON DI LEO, J., BACCHI, F.A., COLMAN, J. & BOLDES, U. 2005 Experimental determination of the influence of turbulent scale on the lift and drag coefficients of low Reynolds number airfoils. *Latin Am. Appl. Res.* 35 (3), 183–188.
- DEVINANT, P., LAVERNE, T. & HUREAU, J. 2002 Experimental study of wind-turbine airfoil aerodynamics in high turbulence. *J. Wind Engng Ind. Aerodyn.* **90** (6), 689–707.
- DIWAN, S.S. & RAMESH, O.N. 2009 On the origin of the inflectional instability of a laminar separation bubble. J. Fluid Mech. 629, 263–298.
- DIWAN, S.S. & RAMESH, O.N. 2012 Relevance of local parallel theory to the linear stability of laminar separation bubbles. J. Fluid Mech. 698, 468–478.
- DOVGAL, A.V., KOZLOV, V.V. & MICHALKE, A. 1994 Laminar boundary layer separation: instability and associated phenomena. *Prog. Aerosp. Sci.* **30** (1), 61–94.
- DRELA, M. 1989 XFOIL: an analysis and design system for low Reynolds number airfoils. In Low Reynolds Number Aerodynamics (ed. J.M. THOMAS), pp. 1–12. Springer Berlin Heidelberg.
- EPPS, B.P. & KRIVITZKY, E.M. 2019 Singular value decomposition of noisy data: mode corruption. *Exp. Fluids* **60** (8), 121.
- FANG, X. & WANG, Z. 2024 On the low-frequency flapping motion in flow separation. J. Fluid Mech. 984, A76.
- FRANSSON, J.H.M. & SHAHINFAR, S. 2020 On the effect of free-stream turbulence on boundary-layer transition. J. Fluid Mech. 899, A23.
- GOMES-FERNANDES, R., GANAPATHISUBRAMANI, B. & VASSILICOS, J.C. 2012 Particle image velocimetry study of fractal-generated turbulence. *J. Fluid Mech.* **711**, 306–336.
- HAIN, R., KÄHLER, C.J. & RADESPIEL, R. 2009 Dynamics of laminar separation bubbles at low-Reynoldsnumber aerofoils. J. Fluid Mech. 630, 129–153.
- HEARST, R.J. & LAVOIE, P. 2015 The effect of active grid initial conditions on high Reynolds number turbulence. *Exp. Fluids* **56** (10), 185.
- HEDLEY, T.B. & KEFFER, J.F. 1974 Turbulent/non-turbulent decisions in an intermittent flow. *J. Fluid Mech.* **64** (4), 625–644.
- HERBST, S.L., HAIN, R. & KÄHLER, C.J. 2020 Low aspect ratio wing under large-scale turbulent inflow conditions at low Reynolds numbers. In *Notes on Numerical Fluid Mechanics and Multidisciplinary Design*, vol. 142, pp. 653–662. Springer Verlag.
- HERBST, S.L., KÄHLER, C.J. & HAIN, R. 2018 Influence of large-scale free-stream turbulence on an SD7003 airfoil at low Reynolds numbers. In 2018 Applied Aerodynamics Conference. American Institute of Aeronautics and Astronautics.
- HERNON, D., WALSH, E.J. & MCELIGOT, D.M. 2007 Experimental investigation into the routes to bypass transition and the shear-sheltering phenomenon. *J. Fluid Mech.* **591**, 461–479.
- Ho, C.-M. & HUERRE, P. 1984 Perturbed free shear layers. Annu. Rev. Fluid Mech. 16 (1), 365-422.

- HOFFMANN, J.A. 1991 Effects of freestream turbulence on the performance characteristics of an airfoil. *AIAA J.* 29 (9), 1353–1354.
- HORTON, H.P. 1968 Laminar separation bubbles in two and three dimensional incompressible flow. PhD thesis, University of London, London.
- HOSSEINVERDI, S. & FASEL, H.F. 2019 Numerical investigation of laminar-turbulent transition in laminar separation bubbles: the effect of free-stream turbulence. *J. Fluid Mech.* **858**, 714–759.
- HRYNUK, J.T., OLSON, D., STUTZ, C. & JACKSON, J. 2024 Effects of turbulence on NACA, 0012 airfoil performance at low Reynolds number. *AIAA J.* 62 (1), 409–417.
- HUNT, J.C.R. 1973 A theory of turbulent flow round two-dimensional bluff bodies. *J. Fluid Mech.* **61** (4), 625–706.
- ISTVAN, M.S., KURELEK, J.W. & YARUSEVYCH, S. 2018 Turbulence intensity effects on laminar separation bubbles formed over an airfoil. *AIAA J.* **56** (4), 1335–1347.
- ISTVAN, M.S. & YARUSEVYCH, S. 2018 Effects of free-stream turbulence intensity on transition in a laminar separation bubble formed over an airfoil. *Exp. Fluids* **59** (3), 52.
- JAROSLAWSKI, T., FORTE, M., VERMEERSCH, O., MOSCHETTA, J.-M. & GOWREE, E.R. 2023 Disturbance growth in a laminar separation bubble subjected to free-stream turbulence. *J. Fluid Mech.* **956**, A33.
- KAY, N.J., RICHARDS, P.J. & SHARMA, R.N. 2020 Influence of turbulence on cambered and symmetrical airfoils at low Reynolds numbers. *AIAA J.* **58** (5), 1913–1925.
- KENDALL, J.M. 1985 Experimental study of disturbances produced in a pre-transitional laminar boundary layer by weak freestream turbulence. In *18th Fluid Dynamics and Plasmadynamics and Lasers Conference*. American Institute of Aeronautics and Astronautics.
- KURELEK, J.W., LAMBERT, A.R. & YARUSEVYCH, S. 2016 Coherent structures in the transition process of a laminar separation bubble. *AIAA J.* 54 (8), 2295–2309.
- LAITONE, E.V. 1997 Wind tunnel tests of wings at Reynolds numbers below 70 000. Exp. Fluids 23 (5), 405–409.
- LANG, M., RIST, U., WAGNER, S., LANG, M. & WAGNER, S. 2004 Investigations on controlled transition development in a laminar separation bubble by means of LDA and PIV. *Exp. Fluids* **36** (1), 43–52.
- LEGRAND, M., NOGUEIRA, J. & LECUONA, A. 2011 Flow temporal reconstruction from non-time-resolved data part I: mathematic fundamentals. Exp. Fluids 51 (4), 1047–1055.
- LENGANI, D. & SIMONI, D. 2015 Recognition of coherent structures in the boundary layer of a low-pressure-turbine blade for different free-stream turbulence intensity levels. *Intl J. Heat Fluid Flow* **54**, 1–13.
- LENGANI, D., SIMONI, D., UBALDI, M. & ZUNINO, P. 2014 POD analysis of the unsteady behavior of a laminar separation bubble. *Exp. Therm. Fluid Sci.* **58**, 70–79.
- LENGANI, D., SIMONI, D., UBALDI, M., ZUNINO, P. & BERTINI, F. 2017 Analysis of the Reynolds stress component production in a laminar separation bubble. *Intl J. Heat Fluid Flow* **64**, 112–119.
- LESIEUR, M. 2008 Turbulence in Fluids. Springer Netherlands.
- LI, L. & HEARST, R.J. 2021 The influence of freestream turbulence on the temporal pressure distribution and lift of an airfoil. J. Wind Engng Ind. Aerodyn. 209, 104456.
- LI, Y., YANO, J.I. & LIN, Y. 2019 Is atmospheric convection organised?: information entropy analysis. Geophys. Astrophys. Fluid Dyn. 113 (5-6), 553–573.
- LITVINENKO, Y.A., CHERNORAY, V.G., KOZLOV, V.V., GREK, G.R., LÖFDAHL, L. & CHUN, H.H. 2005 Adverse pressure gradient effect on nonlinear varicose instability of a streaky structure in an unswept wing boundary layer. *Phys. Fluids* 17 (11), 1–3.
- MAHALLATI, A., MCAULIFFE, B.R., SJOLANDER, S.A. & PRAISNER, T.J. 2012 Aerodynamics of a low-pressure turbine airfoil at low Reynolds numbers-part I: steady flow measurements. *J. Turbomach.* **135** (1), 1–9
- MALDONADO, V., CASTILLO, L., THORMANN, A. & MENEVEAU, C. 2015 The role of free stream turbulence with large integral scale on the aerodynamic performance of an experimental low Reynolds number S809 wind turbine blade. *J. Wind Engng Ind. Aerodyn.* 142, 246–257.
- MAMIDALA, S.B., WEINGÄRTNER, A. & FRANSSON, J.H.M. 2022 Leading-edge pressure gradient effect on boundary layer receptivity to free-stream turbulence. *J. Fluid Mech.* 935.
- MANDAL, A.C., VENKATAKRISHNAN, L. & DEY, J. 2010 A study on boundary-layer transition induced by free-stream turbulence. *J. Fluid Mech.* **660**, 114–146.
- MARCHMAN, J.F. 1987 Aerodynamic testing at low Reynolds numbers. J. Aircraft 24 (2), 107–114.
- MARXEN, O. & HENNINGSON, D.S. 2011 The effect of small-amplitude convective disturbances on the size and bursting of a laminar separation bubble. *J. Fluid Mech.* **671**, 1–33.
- MARXEN, O., LANG, M. & RIST, U. 2013 Vortex formation and vortex breakup in a laminar separation bubble. J. Fluid Mech. 728, 58–90.

- MATSUBARA, M. & ALFREDSSON, P.H. 2001 Disturbance growth in boundary layers subjected to free-stream turbulence. *J. Fluid Mech.* **430**, 149–168.
- MEINHART, C.D., WERELEY, S.T. & SANTIAGO, J.G. 2000 A piv algorithm for estimating time-averaged velocity fields. *J. Fluids Engng Trans. ASME* 122 (2), 285–289.
- MICHELIS, T., YARUSEVYCH, S. & KOTSONIS, M. 2017 Response of a laminar separation bubble to impulsive forcing. *J. Fluid Mech.* **820**, 633–666.
- MICHELIS, T., YARUSEVYCH, S. & KOTSONIS, M. 2018 On the origin of spanwise vortex deformations in laminar separation bubbles. *J. Fluid Mech.* 841, 81–108.
- MOFFAT, R.J. 1988 Describing the uncertainties in experimental results. Exp. Therm. Fluid Sci. 1 (1), 3-17.
- MUELLER, T.J. & DELAURIER, J.D. 2003 Aerodynamics of small vehicles. *Annu. Rev. Fluid Mech.* **35** (1), 89–111.
- NAGARAJAN, S., LELE, S.K. & FERZIGER, J.H. 2007 Leading-edge effects in bypass transition. *J. Fluid Mech.* 572, 471–504.
- NOLAN, K.P. & WALSH, E.J. 2012 Particle image velocimetry measurements of a transitional boundary layer under free stream turbulence. J. Fluid Mech. 702, 215–238.
- OHTAKE, T., NAKAE, Y. & MOTOHASHI, T. 2007 Nonlinearity of the aerodynamic characteristics of NACA0012 aerofoil at low Reynolds numbers. *J. Japan Soc. Aeronaut. Space Sci.* 55 (644), 439–445.
- OL, M., McCauliffe, B., Hanff, E., Scholz, U. & Kähler, C.J. 2005 Comparison of laminar separation bubble measurements on a low Reynolds number airfoil in three facilities. In 35th AIAA Fluid Dynamics Conference and Exhibit. American Institute of Aeronautics and Astronautics.
- OVCHINNIKOV, V., CHOUDHARI, M.M. & PIOMELLI, U. 2008 Numerical simulations of boundary-layer bypass transition due to high-amplitude free-stream turbulence. *J. Fluid Mech.* **613**, 135–169.
- PARK, D., SHIM, H. & LEE, Y. 2020 PIV measurement of separation bubble on an airfoil at low Reynolds numbers. *J. Aerospace Engng* **33** (1), 1–17.
- RAVI, S., WATKINS, S., WATMUFF, J., MASSEY, K., PETERSON, P. & MARINO, M. 2012 Influence of large-scale freestream turbulence on the performance of a thin airfoil. *AIAA J.* **50** (11), 2448–2459.
- REED, H.L., SARIC, W.S. & ARNAL, D. 1996 Linear stability theory applied to boundary layers. Annu. Rev. Fluid Mech. 28 (1), 389–428.
- RESHOTKO, E. 2001 Transient growth: a factor in bypass transition. Phys. Fluids 13 (5), 1067-1075.
- REUSS, D.L., ADRIAN, R.J., LANDRETH, C.C., FRENCH, D.T. & FANSLER, T.D. 1989 Instantaneous planar measurements of velocity and large-scale vorticity and strain rate in an engine using particle-image velocimetry. SAE Technical Papers, vol. 98.
- SARIC, W.S., REED, H.L. & KERSCHEN, E.J. 2002 Boundary-layer receptivity to freestream disturbances. *Annu. Rev. Fluid Mech.* **34** (1), 291–319.
- SCARANO, F. & RIETHMULLER, M.L. 2000 Advances in iterative multigrid PIV image processing. Exp. Fluids 29 (7), S051–S060.
- SCHLICHTING, H. & GERSTEN, K. 2017 Boundary-Layer Theory. 9th edn. Springer Berlin Heidelberg.
- SCHRADER, P. 1993 Computing the statistical stability of integral length scale measurements by autoregressive simulation. *J. Wind Engng Ind. Aerodyn.* **46–47** (6), 487–496.
- SCIACCHITANO, A. & WIENEKE, B. 2016 PIV uncertainty propagation. Meas. Sci. Technol. 27 (8), 084006.
- SERNA, J. & LAZARO, B.J. 2015 On the bursting condition for transitional separation bubbles. *Aerosp. Sci. Technol.* **44**, 43–50.
- SHANNON, C.E. 1949 Communication in the presence of noise. Proc. IRE 37 (1), 10-21.
- SICOT, C., AUBRUN, S., LOYER, S. & DEVINANT, P. 2006 Unsteady characteristics of the static stall of an airfoil subjected to freestream turbulence level up to 16 %. Exp. Fluids 41 (4), 641–648.
- SIMONI, D., LENGANI, D., UBALDI, M., ZUNINO, P. & DELLACASAGRANDE, M. 2017 Inspection of the dynamic properties of laminar separation bubbles: free-stream turbulence intensity effects for different Reynolds numbers. Exp. Fluids 58 (6), 66.
- SIROVICH, L. 1987 Turbulence and the dynamics of coherent structures. I. Coherent structures. Q. Appl. Maths 45 (3), 561–571.
- SYTSMA, M.J. & UKEILEY, L. 2013 Mean loads from wind-tunnel turbulence on low-aspect-ratio flat plates. J. Aircraft 50 (3), 863–870.
- TAIRA, K., BRUNTON, S.L., DAWSON, S.T.M., ROWLEY, C.W., COLONIUS, T., MCKEON, B.J., SCHMIDT, O.T., GORDEYEV, S., THEOFILIS, V. & UKEILEY, L.S. 2017 Modal analysis of fluid flows: an overview. *AIAA J.* 55 (12), 4013–4041.
- TANI, I. 1964 Low-speed flows involving bubble separations. *Prog. Aerosp. Sci.* 5, 70–103.
- TAYLOR, G.I. 1938 The spectrum of turbulence. Proc. R. Soc. A: Math. Phys. Engng Sci. 164 (919), 476–490.

- THOMPSON, C., BILER, H., SYMON, S. & GANAPATHISUBRAMANI, B. 2023 Effects of integral length scale variations on the stall characteristics of a wing at high free-stream turbulence conditions. *J. Fluid Mech.* **974.** A9.
- TOPPINGS, C.E. & YARUSEVYCH, S. 2022 Structure and dynamics of a laminar separation bubble near a wing root: towards reconstructing the complete LSB topology on a finite wing. *J. Fluid Mech.* **944**, A14.
- TOPPINGS, C.E. & YARUSEVYCH, S. 2023 Transient dynamics of laminar separation bubble formation and bursting. *Exp. Fluids* **64** (3), 57.
- TOPPINGS, C.E. & YARUSEVYCH, S. 2024 Laminar separation bubble formation and bursting on a finite wing. *J. Fluid Mech.* **986**, A26.
- URUBA, V. 2019 Energy and entropy in turbulence decompositions. Entropy 21 (2), A30.
- VALENTE, P.C. & VASSILICOS, J.C. 2011 The decay of turbulence generated by a class of multiscale grids. J. Fluid Mech. 687, 300–340.
- VITA, G., HEMIDA, H., ANDRIANNE, T. & BANIOTOPOULOS, C. 2020 The effect of the integral length scale of turbulence on a wind turbine aerofoil. *J. Wind Engng Ind. Aerodyn.* **204**, 104235.
- WANG, R. & XIAO, Z. 2021 Influence of free-stream turbulence on the aerodynamic performance of a threedimensional airfoil. AIP Adv. 11, 075304.
- WANG, S., ZHOU, Y., ALAM, M.M. & YANG, H. 2014 Turbulent intensity and Reynolds number effects on an airfoil at low Reynolds numbers. *Phys. Fluids* **26**, 115107.
- WATKINS, S., MILBANK, J., LOXTON, B.J. & MELBOURNE, W.H. 2006 Atmospheric winds and their implications for microair vehicles. *AIAA J.* 44 (11), 2591–2600.
- WATKINS, S., RAVI, S. & LOXTON, B. 2010 The effect of turbulence on the aerodynamics of low Reynolds number wings. *Engng Lett.* **18** (3), 9.
- WATMUFF, J.H. 1999 Evolution of a wave packet into vortex loops in a laminar separation bubble. *J. Fluid Mech.* **397**, 119–169.
- WELCH, P. 1967 The use of fast Fourier transform for the estimation of power spectra: a method based on time averaging over short, modified periodograms. *IEEE Trans. Audio Electroacoust.* **15** (2), 70–73.
- WESTERWEEL, J. & SCARANO, F. 2005 Universal outlier detection for PIV data. Exp. Fluids 39 (6), 1096–1100.
- WIENEKE, B. 2015 PIV uncertainty quantification from correlation statistics. Meas. Sci. Technol. 26 (7), 074002.
- WINSLOW, J., OTSUKA, H., GOVINDARAJAN, B. & CHOPRA, I. 2018 Basic understanding of airfoil characteristics at low Reynolds numbers (104–105). J. Aircraft 55 (3), 1050–1061.
- WOOD, D.H. 2011 Small wind turbines. In Advances in Wind Energy Conversion Technology, pp. 195–211.Springer-Verlag.
- WYNGAARD, J.C. 1992 Atmospheric turbulence. Annu. Rev. Fluid Mech. 24 (1), 205–234.
- YARAS, M.I. 2002 Measurements of the effects of freestream turbulence on separation-bubble transition. In *Volume 3: Turbo Expo 2002, Parts A and B*, vol. 3 A, pp. 647–660. ASMEDC.
- YARUSEVYCH, S., SULLIVAN, P.E. & KAWALL, J.G. 2009 On vortex shedding from an airfoil in low-Reynolds-number flows. *J. Fluid Mech.* **632**, 245–271.
- YAVUZKURT, S. 1984 A guide to uncertainty analysis of hot-wire data. J. Fluids Engng 106 (2), 181–186.
- YU, M., HRYNUK, J.T., BOOTH, D.T. & POUDEL, N. 2024 Freestream turbulence effects on low Reynolds number NACA 0012 airfoil laminar separation bubble and lift generation. *Aerosp. Sci. Technol.* **149**, 109145.
- ZHAO, Y. & SANDBERG, R.D. 2020 Bypass transition in boundary layers subject to strong pressure gradient and curvature effects. *J. Fluid Mech.* 888, A4.